THE ASTROPHYSICAL JOURNAL, 550:668–690, 2001 April 1

THE NUCLEAR DYNAMICS OF M32. I. DATA AND STELLAR KINEMATICS[1]

C. L. JOSEPH,[2] D. MERRITT,[2] R. OLLING,[2] M. VALLURI,[2,3] R. BENDER,[4] G. BOWER,[5] A. DANKS,[6] T. GULL,[7] J. HUTCHINGS,[8] M. E. KAISER,[9] S. MARAN,[7] D. WEISTROP,[10] B. WOODGATE,[7] E. MALUMUTH,[7] C. NELSON,[10] P. PLAIT,[7] AND D. LINDLER[11]

Received 2000 May 25; accepted 2000 November 10

ABSTRACT

We have obtained optical long-slit spectroscopy of the nucleus of M32 using the Space Telescope Imaging Spectrograph aboard the *Hubble Space Telescope*. The stellar rotation velocity and velocity dispersion, as well as the full line-of-sight velocity distribution (LOSVD), were determined as a function of position along the slit using two independent spectral deconvolution algorithms. We see three clear kinematical signatures of the nuclear black hole: a sudden upturn, at $\sim 0\farcs3$ from the center, in the stellar velocity dispersions; a flat or rising rotation curve into the center; and strong, non-Gaussian wings on the central LOSVD. The central velocity dispersion is ~ 130 km s^{-1} (Gaussian fit) or $\gtrsim 175$ km s^{-1} (corrected for the wings). The central kinematics are consistent with the presence of a supermassive compact object in M32 with a mass in the range $(2\text{–}4) \times 10^6\ M_\odot$.

Subject headings: celestial mechanics, stellar dynamics — galaxies: elliptical and lenticular, cD — galaxies: individual (M32) — galaxies: kinematics and dynamics — galaxies: nuclei — galaxies: structure

1. INTRODUCTION

The presence of a supermassive compact object, presumably a black hole, at the center of the dwarf elliptical galaxy M32 has been suspected for some time (Tonry 1987). The evidence consists of rapid rotation of the stars near the center of M32 and a central peak in the stellar velocity dispersions (Tonry 1987; Dressler & Richstone 1988; Carter & Jenkins 1993; van der Marel et al. 1994a; Bender, Kormendy, & Dehnen 1996). The most recent study (van der Marel et al. 1997a, 1997b, 1998) used data from the Faint Object Spectrograph (FOS) on the *Hubble Space Telescope* (*HST*) to infer the rotation and dispersion velocities with a spatial resolution of $\sim 0\farcs1$ in the inner $\sim 0\farcs5$ of M32. The FOS data revealed a sharper rise in the stellar velocity dispersions than had been observed from the ground, thus strengthening the case for a supermassive black hole in M32, of mass $M_h \approx 3 \times 10^6\ M_\odot$.

Here we present observations of M32 carried out using the Space Telescope Imaging Spectrograph (STIS), on *HST*. Our data were obtained as part of the STIS Investigation Definition Team's (IDT) key program to observe the nuclei of a sample of ~ 15 nearby galaxies in the spectral region centered on the calcium triplet, $\lambda \approx 8600$ Å. This paper is the first in a series that will present stellar-kinematical evidence from STIS for the presence (or absence) of supermassive black holes in galactic nuclei.

The STIS data improve on earlier ground-based and FOS data from M32 in several ways. The spatial resolution of STIS is $\sim 0\farcs1$, or ~ 0.3 pc at the distance of M32, similar to that of the single FOS aperture; however STIS provides continuous spatial sampling along a slit. The spectral resolution of STIS in the G750M mode (~ 38 km s^{-1}) is much greater than that of the FOS making STIS a more suitable instrument for observing M32, whose velocity dispersion outside of the nucleus is only ~ 60 km s^{-1}. We were able to obtain from the STIS spectra not only the lowest-order moments of the stellar velocity distribution—the rotation velocity and velocity dispersion—but also the full line-of-sight velocity distribution (LOSVD) as a function of position along the major axis.

A number of modeling studies (van der Marel et al. 1994b; Dehnen 1995; Qian et al. 1995) have made predictions about the observable signatures at *HST* resolution of a supermassive black hole in M32. The black hole is expected to be associated with three kinematical features. (1) The stellar rotation velocity should remain flat, or rise slightly, as one approaches the center from either side, before falling to zero in the central pixel. (2) The stellar velocity dispersion should exhibit a sudden upturn at a distance of $\sim 0\farcs2$–$0\farcs5$ from the center, reaching a central value of ~ 120 km s^{-1} or greater depending on the mass of the black hole. (3) The distribution of line-of-sight stellar velocities in the resolution element centered on the black hole should be strongly non-Gaussian, with extended, high-velocity wings. Part of the predicted rise in the velocity dispersion near the center would be due to these wings; part to blending of the rotation curve from the two sides of the galaxy; and part to an intrinsic rise in the random velocities.

We see all three signatures of the black hole in the STIS data. The velocity dispersion spike is most impressive. In

[1] Based on observations with the NASA/ESA *Hubble Space Telescope*, obtained at the Space Telescope Science Institute, which is operated by the Association of Universities for Research in Astronomy (AURA), Inc., under NASA contract NAS 5-26555.

[2] Department of Physics and Astronomy, Rutgers University, New Brunswick, NJ 08855.

[3] Astronomy and Astrophysics, University of Chicago, 5640 South Ellis Avenue, Chicago, IL 60637.

[4] Universitäts-Sternwarte, Scheinerstrasse 1, München 81679, Germany.

[5] NOAO, P.O. Box 26732, Tucson, AZ 85726.

[6] RPSC Goddard Space Flight Center, Code 683, Greenbelt, MD 20771.

[7] NASA Goddard Space Flight Center, Code 681, Greenbelt, MD 20771.

[8] Dominion Astrophysical Observatory, 5071 West Saanich Road, Victoria, BC V8X 4M6, Canada.

[9] Johns Hopkins University, Department of Physics and Astronomy, 34th and Charles Street, Baltimore, MD 21218.

[10] University of Nevada, Department of Physics, 4505 South Maryland Parkway, Las Vegas, NV 89154.

[11] Advanced Comp. Concepts, Inc., 11518 Gainsborough Road, Potomac, MD 20854.

terms of the usual parametrization σ_0 (the dispersion of the Gaussian core of the LOSVD), the central measured value is ~ 130 km s^{-1}. Correcting σ for the non-Gaussian wings of the LOSVD gives a considerably greater value, at least 175 km s^{-1}, or ~ 3 times the value in the main body of M32. We argue that most of the central upturn in the stellar velocity dispersion reflects a true increase in the random component of the stellar motion and not simply a blending of the rotation curve from the two sides of the nucleus.

We adopt a distance to M32 of 0.7 Mpc; thus 1″ corresponds to 3.25 pc.

2. OBSERVATIONS AND DATA REDUCTION

M32 was observed on 1998 September 4 with STIS in the long-slit mode with wavelength centered near the Ca II triplet feature at 8561 Å. STIS is described by Woodgate et al. (1998) and its on-orbit performance by Kimble et al. (1998). The present data are part of a survey of the nuclei of nearby galaxies being conducted by the STIS IDT (*HST* Program ID 7566). The goal of the survey is to place stellar kinematical constraints on the masses of nuclear black holes. Two orbits of data with a total integration time of 4898 s were obtained. The *HST* spacecraft tracking was operated in fine lock with a reported jitter of no more than 3 mas rms or 11 mas peak to peak. The aperture was 52″ × 0.″1 with a position angle of 163°, coincident with the M32 isophotal major axis. The CCD data were read out in the unbinned mode. Spatial sampling at the focal plane was at every 0.″05071, corresponding to a 2 pixel optical resolution of about 0.″115 FWHM (see Table 1). Outside of ±0.″7, the data were binned spatially to enhance the signal. The spectral resolution was approximately 38 km s^{-1}. M32 spectra were obtained in the CR-split mode to assist with cosmic-ray (CR) identification and rejection. The location of the galaxy center in the image was moved by approximately 4.5 rows along the aperture between the two orbits to ensure that residual detector sensitivity variations, which may not be completely removed from the data during reduction, are not mistaken for weak features. This form of dithering also assists with the identification of hot pixels in the CCD which do not rectify well.

A spectrum of the star HR 7615 was obtained with the same STIS aperture earlier in the program (Fig. 1). This bright, K0 III giant was used as the primary template for extracting the LOSVD of the stars in M32 from the STIS spectra. Spectra of two other stars (spectral types G8 and K3) were also obtained and used to test the sensitivity of the spectral deconvolution to template mismatch, as described below. A set of spectral images of HR 7615 were taken centered at −0.″05, 0.″00, and +0.″05 with respect to the centerline of the aperture (i.e., offset along the dispersion direction). These data were added together using appropriate weights to match the aperture illumination profile of M32. Each of these spectral images has a slightly different shift in its velocity centroid and the combined image provides a more accurate template for determining the kinematics of an extended object such as a galaxy. Internal wavelength calibration images ("wavecals") as well as an internal continuum lamp image ("flat field") were taken for calibration purposes. An image that has had all of the instrumental response removed is said be a rectified image. The contemporaneous flat field spectrum was obtained in the portion of the orbit where HR 7615 was behind the Earth. The flat spectrum was taken through the 0.″2 × 0.″09 aperture rather than through the long aperture since the former is superior for removing the pixel-to-pixel detector response of a stellar point source. A contemporaneous flat field was used to remove the internal fringing which is significant for wavelengths greater than 7500 Å and which changes over time (Goudfrooij, Baum, & Walsh 1997). We note that the fringing is far more serious for low-dispersion spectra especially for high signal-to-noise ratios (S/Ns) than it is for our data taken in medium dispersion.

TABLE 1

OBSERVATIONAL SETUP

Parameter	Value
Gain (e^- ADU^{-1})	1.0
Wavelength coverage (Å)	8275–8847
Reciprocal dispersion (Å pixel^{-1})	0.56
Aperture	52″ × 0.″1
Comparison line FWHM (pixels)	2.0
$R = \lambda/\Delta\lambda$	7644
Instrumental dispersion (σ_I) (km s^{-1})	17.1
Spatial scale (arcsec pixel^{-1})	0.05071

Cosmic rays account for approximately 20% of the total signal and contaminate approximately 5% of the pixels in a typical exposure. CRs were identified and removed using the following procedure. The centroids in the cross-dispersion direction were determined for each rectified image and the images shifted so that the galaxy core appeared on the same row. CRs were identified and removed by comparing the flux in a given pixel to the flux in the corresponding pixel in subsequent images. For each pixel, outlying values were rejected and excluded when the frames were averaged together. Our data set for M32 included four raw images. Most pixels were found to have four frames contributing to their average values, while fewer pixels had three or fewer frames. Only 2 pixels within the central 2″ had contributions from no frames. Those pixels were assigned values representing the average of their adjacent pixels.

The M32 data were reduced using two separate approaches: (1) "shift and add," and (2) "frame by frame." The latter relies heavily on a standard software package called CALSTIS at Goddard Space Flight Center. The shift-and-add method starts by removing the detector response using contemporaneous flat, bias, and dark calibration files. CR hits are then removed using the procedure described previously. The frames are averaged together and the resulting frame is remapped to place the spectra from a single location along the aperture onto a single row. As with most spectrographs, STIS produces spectra with S-shaped and pincushion distortions, as well as spectra that are not aligned exactly with a row. A cubic interpolation was used to remap the spectra for later analysis. The remapping is not perfect, with centroid errors of approximately 0.1 pixel rms. This level of accuracy was deemed adequate, although we are working to improve it. In addition, the remapping produces very minor ($\lesssim 1\%$) residual moiré ripples in the data, which can be minimized but not completely eliminated. Further work is also underway to measure and correct for this residual affect. The strength of the shift-and-add technique is that it preserves photometric accuracy. However, it has the disadvantage of introducing a subpixel image smearing since each frame is registered to the nearest integer pixel.

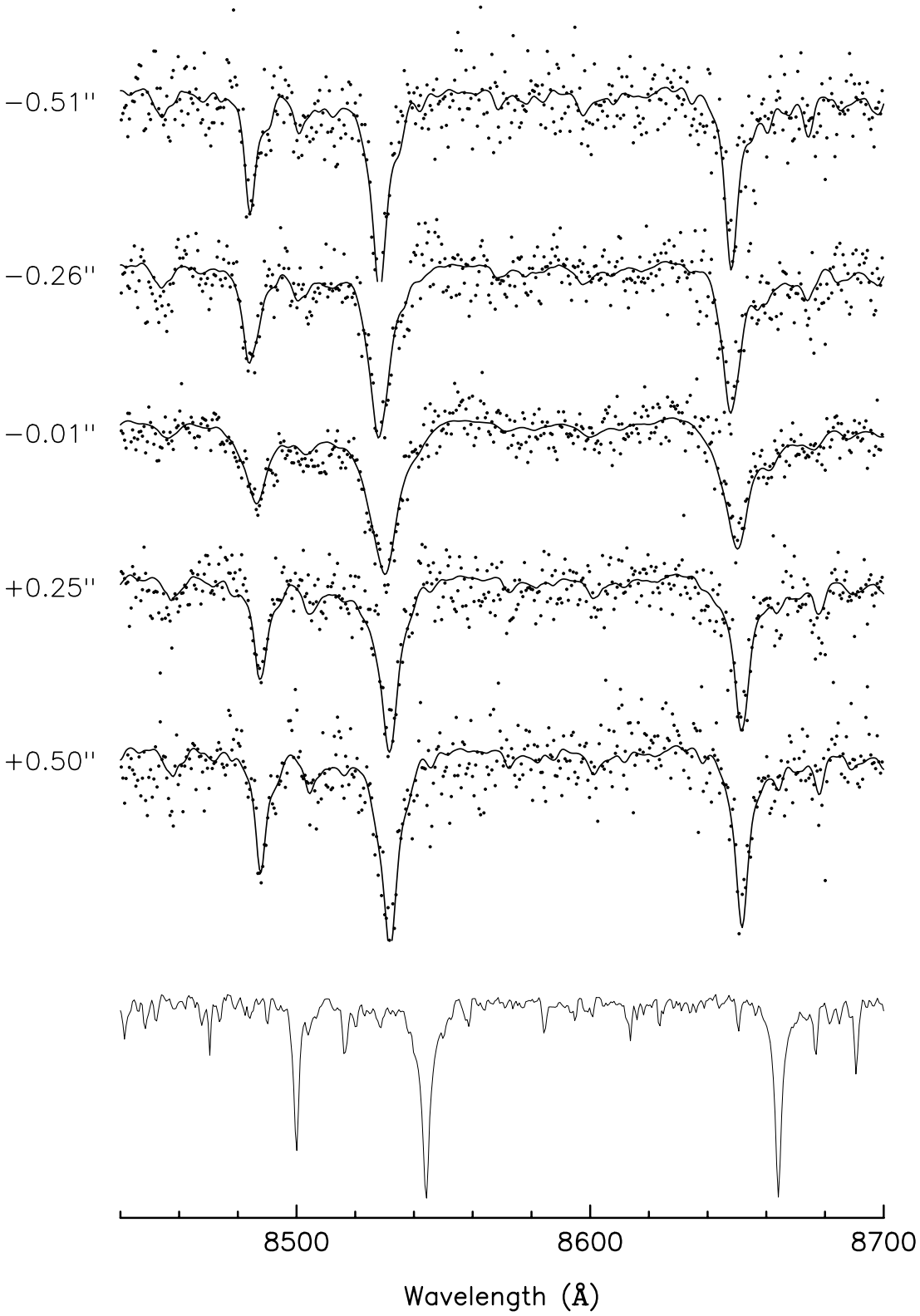

FIG. 1.—*Top*: STIS spectra of M32 at five positions along the slit. Solid curves are convolutions of the MPL-derived broadening functions $\hat{N}(V)$ (Fig. 4) with the stellar template. *Bottom*: Spectrum of HR 7615, a K0 III giant, the template spectrum. The vertical scale of the template spectrum is compressed with respect to that of the M32 spectra.

The philosophy of the frame-by-frame method is to apply all calibration corrections (including the remapping described above) to a single frame before the resulting frames are added together. This approach has the advantage of preserving the highest spatial resolution. However, a substantial fraction of the pixels in each frame in this case are interpolated values, potentially sacrificing some photometric precision. As noted above, CRs contaminate approximately 5% of the pixels in a 20 minute exposure. After remapping, as many as 20% of the pixels must be assigned a

reduced weight for the final averaging since a single pixel often gets remapped partially into several pixels in the new image.

Fortunately, both approaches to the data reduction were found to give very similar results. While the frame-by-frame method produced a higher apparent S/N than the shift-and-add method, the former method is more prone to the introduction of systematic error. We adopted the more conservative approach of accepting a somewhat higher variance rather than risk the introduction of a bias. We therefore adopted the shift-and-add spectra for the analysis of the LOSVDs in the present study. Figure 1 shows spectra at several positions along the aperture. As noted above, we are continuing in our efforts to refine the data reduction techniques still further.

3. RECOVERY OF THE STELLAR VELOCITY DISTRIBUTION

3.1. *Method*

An observed spectrum $I(\lambda)$ is the convolution of the line-of-sight velocity distribution $N(V)$ of the stars within the aperture with the spectrum of a single star $T(\lambda)$:

$$I(\ln \lambda) = \int N(V)T(\ln \lambda - V/c)dV \ . \qquad (1)$$

The goal is to extract an estimate $\hat{N}(V)$ of the true stellar broadening function $N(V)$ given $I(\lambda)$ and $T(\lambda)$, both observed with the same instrument.

Two independent deconvolution routines were used. The first algorithm, the "Fourier correlation quotient" (FCQ) method (Bender 1990; Bender, Saglia, & Gerhard 1994), constructs an estimate of the broadening function using Fourier techniques. The FCQ routine differs from earlier Fourier algorithms (e.g., Sargent et al. 1977) in that the deconvolution is based on the template-galaxy correlation function rather than on the spectra themselves. This approach is less sensitive to template mismatch (Bender 1990). The second algorithm, "maximum penalized likelihood" (MPL), finds $\hat{N}(V)$ as the solution to a penalized likelihood problem. The MPL estimate of $N(V)$ is computed on a grid in V in such a way as to optimize the fit of the convolved template to the galaxy spectrum, subject to a "penalty" that measures the lack of smoothness of $\hat{N}(V)$ (Merritt 1997).

Both algorithms are nonparametric in the sense that no explicit constraints are placed on the functional form of $\hat{N}(V)$. However they differ in two ways that are important for the current study. The FCQ algorithm requires that the absorption lines in the template spectrum be narrow compared to the broadened lines of the galaxy spectrum, i.e., that the galaxy velocity dispersion be large compared to the instrumental resolution. The MPL routine works well even when the galaxy velocity dispersion is small, as long as both template and galaxy spectra are observed at the same spectral resolution, at least in the case that the template star and galaxy have the same intrinsic absorption line properties.

The two algorithms differ also in the way they deal with the amplification of noise that accompanies the deconvolution. The FCQ routine uses a Wiener filter to suppress high-frequency components of the template-galaxy correlation function $\tilde{K}_{T,G}$. The degree of smoothing is determined by a factor, called here W, which fixes the width of the Gaussian function used to model the low-frequency, or signal, component of $\tilde{K}_{T,G}$. The choice $W = 1$ corresponds to "optimal" filtering and larger values produce less smoothing; the FCQ algorithm adopts a default value of $W = 1$, but automatically increases W (to a maximum of 1.3) if the recovered LOSVD shows evidence of significantly non-Gaussian wings. In the MPL algorithm, the level of smoothing is determined by a factor α that multiplies the smoothness penalty function. The appropriate penalty function to use is the one that assigns the least penalty to whatever class of smooth functions best describe the data. In our case, the LOSVDs are expected to be approximately Gaussian, hence we adopt Silverman's (1982) prescription which assigns zero penalty to any Gaussian $N(V)$. The use of Silverman's penalty function is expected to produce less bias than simpler penalty functions based on the mean-square second derivative, which assign a nonzero penalty even to Gaussian functions (e.g., Gebhardt et al. 2000). However, there is no a priori way of estimating the optimum value of α in the MPL algorithm.

The different effects of smoothing on the form of $\hat{N}(V)$ are illustrated in Figure 2, which shows estimates of the LOSVD in the central resolution element of M32 as computed by the two routines. Both algorithms produce rapidly fluctuating solutions when undersmoothed, a consequence of the amplification of noise that accompanies deconvolution. The only significant difference in this regime is the nonnegativity of the MPL estimates, a consequence of the logarithmic form of the penalty function (Silverman 1982). As the smoothing is increased, systematic differences begin to appear which are related to the different smoothing algorithms in the two codes. Solutions obtained via MPL tend to be more robust with respect to the degree of smoothing, producing in the limit of large α a Gaussian fit. However Figure 2 suggests that estimates of certain quantities, e.g., the wings of the LOSVD, might depend sensitively on the choice of smoothing level in either algorithm.

Once an estimate of $N(V)$ has been obtained, various quantities related to the line-of-sight velocity distribution can be derived. The simplest of these are the mean and rms velocities, which we denote by $\overline{V}$ and σ, respectively. As is well known, both quantities are difficult to estimate for numerically recovered LOSVDs since they are sensitively dependent on the form of $\hat{N}(V)$ at large velocities where this function is most poorly determined. A standard alternative is to describe $\hat{N}(V)$ by a Gram-Charlier or Gauss-Hermite (GH) series, the product of a normalizing Gaussian with a sum of Hermite polynomials H_i, both expressed in terms of $(V - V_0)/\sigma_0$ (Thompson & Tapia 1990). The parameters V_0 and σ_0 take the place of $\overline{V}$ and σ; while their definitions are to an extent arbitrary, these two parameters are typically determined by requiring the coefficients of H_1 and H_2, called h_1 and h_2, to be zero (Gerhard 1993; van der Marel & Franx 1993). Because V_0 and σ_0 describe the Gaussian core of the LOSVD, they are relatively insensitive to deviations of $\hat{N}(V)$ from Gaussianity at high velocities. Information about these deviations is contained in the higher order coefficients h_3, h_4, etc.; h_3 measures asymmetries in $N(V)$ and h_4 measures the strength of symmetric, non-Gaussian wings.

The FCQ and MPL algorithms derive the GH parameters from $\hat{N}(V)$ in slightly different ways; details are given in Appendix A.

When applied to the STIS M32 spectra, the two algorithms were found to give consistent results for the lowest moments of $N(V)$, i.e., V_0, σ_0, and h_3. However, the

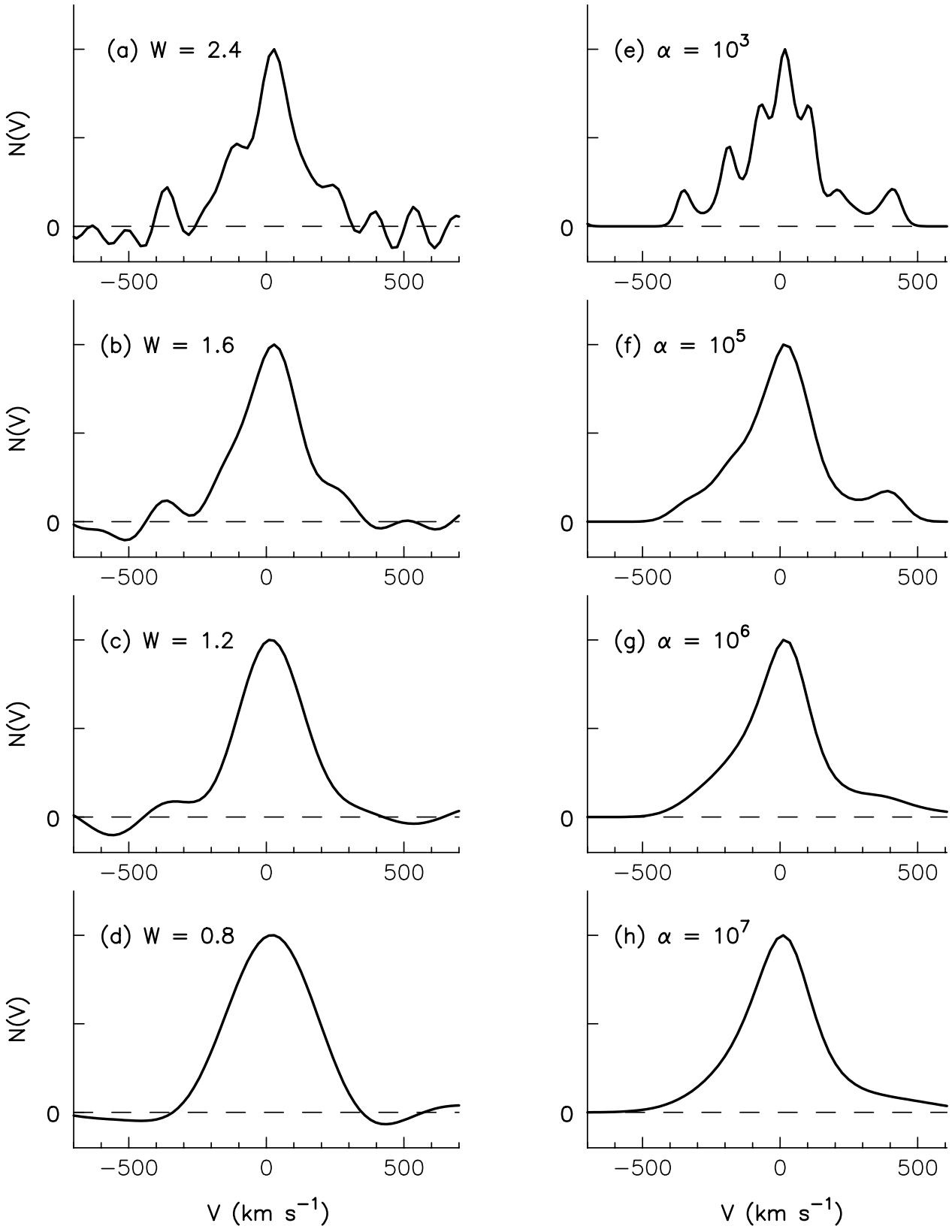

FIG. 2.—Broadening functions recovered from the central spectrum of M32 using the two spectral deconvolution algorithms discussed in the text. The degree of smoothing increases downward. *Left column*: FCQ. (*a*) $W = 2.4$; (*b*) $W = 1.6$; (*c*) $W = 1.2$; (*d*) $W = 0.8$. *Right column*: MPL. (*e*) $\alpha = 10^3$; (*f*) $\alpha = 10^5$; (*g*) $\alpha = 10^7$; (*h*) $\alpha = 10^9$. The MPL estimates tend toward a Gaussian for large α while the FCQ estimates become increasingly distorted as the smoothing is increased. This is the source of the greater bias in the FCQ estimates (although in practice smoothing parameters as small as $W = 0.8$ would never be used).

estimates of h_4 differed significantly at positions outside of the central $\sim 0''.1$. The FCQ algorithm gave $-0.15 \lesssim \hat{h}_4 \lesssim 0$ at almost all positions; negative values of h_4 imply an $N(V)$ that falls off more sharply than a Gaussian at large velocities. The MPL algorithm gave values for h_4 in the range $0 \lesssim h_4 \lesssim 0.1$, corresponding to LOSVDs with super-Gaussian wings. Positive values of h_4 are expected near a black hole (Bahcall & Wolf 1976; van der Marel 1994) and are also characteristic of models with radially anisotropic velocity distributions.

We discuss the origin of this discrepancy in Appendix B. We believe that the primary reason for the systematic difference in $\hat{h}_4$ values is the low velocity dispersion of M32 outside of the very center. When a galaxy's velocity dispersion is comparable to the dispersion of the template star spectrum (~ 50 km s^{-1} in the case of HR 7615), the FCQ algorithm has difficulty recovering the true LOSVD (Figs. 3 and 13; Bender, Paquet, & Nieto 1991). The $\hat{N}(V)$'s recovered by FCQ in this regime are more sharply truncated than the true $N(V)$'s, leading to systematically low estimates of $\hat{h}_4$. For values of σ_0 and S/N comparable to those of M32 at $\sim 1''$, Figure 13 shows that the estimates of h_4 generated by FCQ depend only weakly on the true h_4, with a bias that approaches -0.1 for a true h_4 of 0.1. The MPL algorithm suffers much less from this bias (Figs. 14, 15, and 16).

Bias in nonparametric function estimates can always be reduced by reducing the degree of smoothing (e.g., Silverman 1986), which in the case of the FCQ algorithm means increasing W. Figure 16, panel *c* suggests that increasing W from its default value of 1 to values of ~ 2 can reduce the bias in FCQ estimates of h_4 by factors of 2 or greater, even when σ_0 is as large as 100 km s^{-1}. We carried out this experiment with the STIS data; the results are shown in Figure 3. The average $\hat{h}_4$ values recovered by FCQ in M32 are indeed dependent on W; a change in W from 1 to 1.5 has the effect of increasing $\langle \hat{h}_4 \rangle$ from ~ -0.08 to $\sim +0.08$.

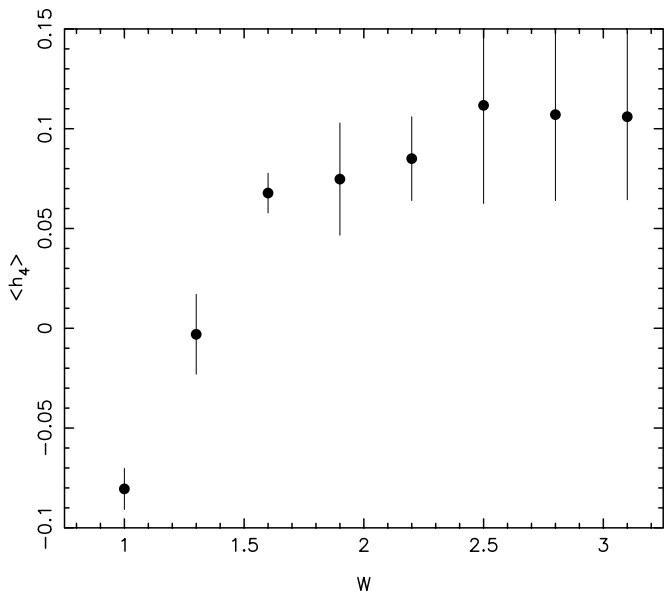

FIG. 3.—Mean value of h_4 computed by the FCQ algorithm between $0''.5$ and $2''.0$, as a function of smoothing parameter W. Large values of W correspond to small degrees of smoothing and, hence, to less biased estimates. These h_4 values are based on data that were heavily binned in radius in order to increase the S/N as much as possible.

The latter value is essentially identical to the mean value of $\hat{h}_4$ recovered via MPL.

The values of $\hat{h}_4$ recovered by MPL are also dependent on the value of the smoothing parameter α but much less so (see Fig. 2), until α is made so large that the LOSVD is forced into a Gaussian shape. The Monte Carlo tests summarized in Figure 16, panel *b* suggest that the bias in $\hat{h}_4$ as recovered by MPL is likely to be only of order ~ -0.02, several times smaller than with FCQ.

We conclude that the values of $\hat{h}_4$ recovered by the two algorithms are consistent once their different biases are taken into account.

3.2. *Results for M32*

The full set of GH parameters derived from the STIS spectra and their 1 σ confidence intervals are given in Table 2 (FCQ) and Table 3 (MPL). For radii $\lesssim 0''.7$ from the center the data were sampled at full resolution ($\sim 0''.05$) while at larger radii they were binned spatially. The sampling at small radii is fine enough that the data points are somewhat correlated; this was done to ensure that no information concerning the steep radial gradients of the profiles was lost.

Figure 4 presents LOSVDs computed via the MPL algorithm at positions separated by about $0''.1$ along the slit. One expects these broadening functions to obey $N(V; R) = N(-V; -R)$, since for a point-symmetric galaxy, the velocity distributions should reverse after passing from one side of the galaxy to the other. The LOSVDs of Figure 4 show approximately the expected symmetry. The right-hand column of Figure 4 plots mean broadening functions averaged over the two sides of the galaxy, $\overline{N}(V) = \frac{1}{2}[N(V, R) + N(-V, -R)]$; the central LOSVD has been symmetrized about $V = 0$.

These broadening functions show clear and consistent deviations from Gaussian form, in two respects. First, the central LOSVD exhibits strong super-Gaussian "wings" at high velocities. These wings are possibly present also in some of the off-center LOSVDs although with lower amplitude. Second, the off-center LOSVDs are asymmetric, with tails extending toward velocities opposite in sign to the mean velocity at each radius. These asymmetric tails are similar to those exhibited by a rotating system superimposed on a slowly rotating bulge.

Figure 5 shows the Gauss-Hermite parameter V_0, a measure of the stellar rotation, in the inner arcsecond of M32. Also plotted are h_3, the lowest, odd GH moment of the LOSVD, and the "corrected" rotation velocity, $V_{0,c} = V_0 + \sqrt{3}\sigma_0 h_3$. $V_{0,c}$ is a closer approximation than V_0 to the true mean line-of-sight velocity $\overline{V}$ (van der Marel & Franx 1993). The corrected rotation velocity is lower in absolute magnitude than $|V_0|$ because of the asymmetric wings of the LOSVD noted above.

The STIS rotation curve is consistent with earlier ground-based measurements (Fig. 7) at radii $\gtrsim 1''$ but with a larger peak value, ~ 60 km s^{-1}. Furthermore the rotation curve remains flat or slightly rising into smaller radii than seen heretofore, before falling at $R \lesssim 0''.25$ as a result of the blending of light from the two sides of the galaxy. There is a suggestion of an east-west asymmetry in the rotation curve though the effect is probably not significant.

The h_3 profile is approximately antisymmetric about the center of M32, as expected in a steady-state galaxy. $|h_3|$ reaches a maximum value of ~ 0.05 at $|R| \approx 0''.3$ and

TABLE 2

M32 KINEMATICS AS DERIVED VIA FCQ

R[a]	V_0[b]	ΔV_0	σ_0[c]	$\Delta\sigma_0$	h_3[d]	Δh_3	h_4[e]	Δh_4	$V_{0,c}$[f]	$\Delta V_{0,c}$	$\sigma_{0,c}$[g]	$\Delta\sigma_{0,c}$
4.497	25.2	32.2	67.2	19.0	0.110	0.436	−0.289	0.436	38.0	60.2	19.6	75.5
4.000	49.7	31.5	97.5	32.2	0.053	0.294	−0.055	0.294	58.7	58.9	84.3	77.3
3.465	55.5	23.6	60.7	13.9	−0.063	0.353	−0.230	0.353	48.8	44.0	26.5	54.9
2.983	54.4	20.6	82.2	18.9	0.017	0.227	−0.090	0.227	56.8	38.3	64.1	49.6
2.546	35.0	18.8	60.1	14.0	0.040	0.284	−0.148	0.284	39.1	35.0	38.3	44.4
2.173	24.1	25.1	103.3	18.7	−0.052	0.221	−0.148	0.221	14.8	46.9	65.9	59.4
1.842	35.9	17.2	64.0	13.0	−0.058	0.245	−0.144	0.245	29.5	32.2	41.4	40.8
1.562	61.5	17.2	88.8	15.6	−0.074	0.176	−0.093	0.176	50.1	32.2	68.6	41.5
1.336	42.8	13.7	76.9	13.5	−0.013	0.162	−0.067	0.162	41.0	25.6	64.3	33.4
1.159	34.4	15.4	81.6	13.9	0.010	0.171	−0.095	0.171	35.8	28.6	62.6	37.0
1.034	53.6	15.3	82.9	12.6	0.059	0.168	−0.122	0.168	62.1	28.6	58.1	36.6
0.932	52.8	13.5	74.4	11.2	−0.024	0.165	−0.120	0.165	49.7	25.2	52.5	32.3
0.831	65.7	12.9	72.2	10.4	−0.078	0.163	−0.129	0.163	55.9	24.2	49.4	30.8
0.729	69.6	11.2	77.1	11.3	−0.001	0.132	−0.057	0.132	69.4	20.9	66.3	27.4
0.654	62.4	12.6	72.5	11.0	0.018	0.158	−0.105	0.158	64.7	23.5	53.9	30.3
0.603	57.5	12.6	79.0	8.1	−0.055	0.144	−0.180	0.144	50.0	23.4	44.2	29.2
0.553	56.8	13.0	75.3	11.1	−0.014	0.157	−0.112	0.157	55.0	24.3	54.7	31.2
0.502	58.8	10.7	72.4	10.1	0.019	0.135	−0.083	0.135	61.1	20.1	57.7	26.1
0.451	58.8	11.6	81.1	11.2	0.000	0.130	−0.074	0.130	58.8	21.6	66.4	28.2
0.401	65.2	10.4	76.0	10.2	−0.089	0.124	−0.065	0.124	53.5	19.4	63.9	25.3
0.350	58.8	10.0	86.0	10.2	−0.067	0.106	−0.055	0.106	48.8	18.7	74.4	24.6
0.299	52.9	9.6	89.3	10.3	−0.072	0.098	−0.037	0.098	41.8	18.0	81.2	23.8
0.248	60.6	8.4	77.4	8.9	−0.041	0.099	−0.044	0.099	55.1	15.7	69.1	20.8
0.198	53.4	8.1	90.4	8.3	−0.049	0.082	−0.057	0.082	45.7	15.2	77.8	20.0
0.147	40.8	9.2	99.4	8.9	0.038	0.084	−0.072	0.084	47.3	17.2	81.8	22.4
0.096	38.9	10.2	112.2	11.2	0.012	0.083	−0.030	0.083	41.2	19.1	104.0	25.4
0.046	36.3	8.7	123.0	10.8	−0.009	0.064	0.019	0.064	34.4	16.2	128.7	22.1
−0.005.....	−2.9	9.0	136.6	12.6	−0.013	0.060	0.075	0.060	−6.0	16.8	161.7	23.8
−0.056.....	−24.6	9.6	124.2	10.1	0.032	0.071	−0.045	0.071	−17.7	18.1	110.5	23.9
−0.106.....	−34.4	9.2	104.2	9.8	0.070	0.081	−0.041	0.081	−21.7	17.3	93.8	22.9
−0.157.....	−40.9	9.9	98.3	11.5	0.087	0.092	−0.007	0.092	−26.1	18.6	96.6	25.0
−0.208.....	−53.1	9.9	90.8	10.4	0.037	0.100	−0.045	0.100	−47.3	18.6	80.8	24.6
−0.259.....	−64.0	9.9	87.3	10.6	0.013	0.103	−0.036	0.103	−62.0	18.4	79.6	24.5
−0.309.....	−62.6	9.0	76.4	8.5	0.052	0.107	−0.079	0.107	−55.7	16.8	61.6	21.8
−0.360.....	−63.4	10.2	80.8	10.8	0.045	0.114	−0.042	0.114	−57.1	18.9	72.5	25.0
−0.411.....	−50.9	12.0	90.4	13.8	0.038	0.120	−0.010	0.120	−44.9	22.3	88.2	30.0
−0.461.....	−57.6	11.6	70.5	11.0	0.016	0.150	−0.078	0.150	−55.7	21.7	57.0	28.2
−0.512.....	−60.1	10.8	63.5	9.0	0.033	0.155	−0.118	0.155	−56.5	20.2	45.1	25.9
−0.563.....	−55.0	13.5	83.4	12.1	0.092	0.147	−0.096	0.147	−41.7	25.2	63.8	32.5
−0.614.....	−51.5	15.5	93.2	15.2	0.047	0.151	−0.067	0.151	−43.9	28.9	77.9	37.8
−0.664.....	−51.4	13.4	66.4	11.6	0.053	0.183	−0.106	0.183	−45.3	25.0	49.2	32.1
−0.715.....	−58.4	13.2	78.0	10.7	0.173	0.154	−0.126	0.154	−35.0	24.8	53.9	31.5
−0.766.....	−46.2	18.0	87.3	17.3	0.189	0.188	−0.076	0.188	−17.6	34.1	71.0	43.9
−0.841.....	−31.8	12.2	77.9	10.1	−0.079	0.142	−0.119	0.142	−42.4	22.7	55.2	29.1
−0.943.....	−51.4	13.4	77.1	11.1	−0.009	0.158	−0.121	0.158	−52.6	25.0	54.3	32.0
−1.044.....	−44.9	13.5	74.9	13.8	0.079	0.164	−0.054	0.164	−34.6	25.3	65.0	33.2
−1.145.....	−48.6	14.9	67.0	11.8	0.037	0.202	−0.132	0.202	−44.3	27.8	45.3	35.4
−1.247.....	−54.2	15.0	73.8	14.1	0.064	0.184	−0.082	0.184	−46.0	27.9	59.0	36.3
−1.372.....	−51.8	23.3	109.2	23.9	−0.044	0.194	−0.053	0.194	−60.1	43.5	95.0	57.2
−1.549.....	−69.3	17.1	83.9	12.4	0.180	0.186	−0.154	0.186	−43.1	32.2	52.3	40.5
−1.778.....	−52.1	16.9	75.6	15.4	−0.075	0.204	−0.092	0.204	−61.9	31.7	58.5	40.9
−2.052.....	−56.6	16.3	81.1	13.5	0.077	0.183	−0.121	0.183	−45.8	30.5	57.1	39.0
−2.382.....	−66.0	18.0	78.2	19.2	0.172	0.209	−0.039	0.209	−42.8	34.0	70.7	44.4
−2.765.....	−54.6	29.4	102.9	29.4	0.048	0.259	−0.061	0.259	−46.1	54.8	87.5	71.7
−3.185.....	−53.9	21.7	62.1	17.2	0.129	0.317	−0.131	0.317	−40.1	40.6	42.2	51.5
−3.673.....	−70.0	51.5	167.0	55.9	−0.003	0.280	−0.033	0.280	−70.8	96.0	153.5	127.6
−4.206.....	−46.9	25.2	30.0	33.3	0.039	0.763	0.047	0.763	−44.9	47.0	33.5	65.3
−4.722.....	−67.4	32.1	6.5	53.7	−0.295	4.505	0.167	4.505	−70.7	65.8	9.1	92.0

[a] Distance from center of M32 in arcseconds.
[b] Rotation parameter V_0 in km s^{-1}.
[c] Dispersion parameter σ_0 in km s^{-1}.
[d] LOSVD skewness parameter h_3.
[e] LOSVD kurtosis parameter h_4.
[f] $V_{0,c} = V_0 + \sqrt{3}\sigma_0 h_3$, an estimate of the true mean line-of-sight velocity.
[g] $\sigma_{0,c} = \sigma_0(1+\sqrt{6}h_4)$, an estimate of the true line-of-sight velocity dispersion.

TABLE 3

M32 KINEMATICS AS DERIVED VIA MPL

R[a]	V_0[b]	ΔV_0	σ_0[c]	$\Delta\sigma_0$	h_3[d]	Δh_3	h_4[e]	Δh_4	$V_{0,c}$[f]	$\Delta V_{0,c}$	$\sigma_{0,c}$[g]	$\Delta\sigma_{0,c}$
4.559	18.9	12.8	51.0	10.4	0.176	0.140	0.022	0.033	34.4	19.7	53.7	12.1
4.184	70.2	18.9	97.2	30.0	−0.235	0.155	0.040	0.079	30.6	51.4	106.7	31.4
3.545	47.3	8.4	47.9	6.8	0.054	0.102	0.008	0.032	51.8	10.1	48.8	8.9
3.068	54.4	8.1	60.3	12.7	−0.054	0.098	0.094	0.033	48.7	14.3	74.2	16.4
2.632	44.8	6.7	45.4	7.0	−0.008	0.111	0.028	0.018	44.1	14.1	48.6	9.6
2.247	27.2	9.8	70.0	10.1	0.043	0.094	0.111	0.060	32.4	12.9	89.0	14.4
1.922	37.6	7.8	62.7	9.0	−0.102	0.080	0.048	0.031	26.5	11.4	70.0	10.1
1.648	71.8	7.9	64.6	12.6	−0.124	0.076	0.080	0.027	57.9	16.7	77.3	16.9
1.415	46.4	6.9	54.8	7.1	−0.008	0.079	0.069	0.023	45.6	10.0	64.1	9.5
1.242	44.7	7.2	64.4	8.6	−0.079	0.091	0.077	0.026	35.9	10.7	76.5	11.6
1.111	49.1	8.1	87.5	11.2	0.070	0.079	0.037	0.047	59.7	13.2	95.5	11.8
1.009	58.2	7.2	72.7	11.2	−0.144	0.087	0.104	0.041	40.1	13.9	91.1	14.1
0.908	71.7	4.6	49.6	6.5	−0.034	0.072	0.036	0.012	68.7	6.7	54.0	8.5
0.806	69.1	4.9	68.7	8.3	0.000	0.070	0.082	0.023	69.1	8.2	82.6	8.7
0.705	49.5	7.0	67.4	8.7	0.138	0.090	0.071	0.026	65.6	13.4	79.1	13.4
0.654	65.3	5.3	64.0	7.1	−0.004	0.060	0.041	0.016	64.9	7.4	70.4	8.5
0.604	68.3	5.2	61.7	7.7	−0.157	0.056	0.051	0.018	51.5	9.3	69.4	8.1
0.553	62.2	5.4	56.3	6.4	−0.034	0.060	0.060	0.019	58.9	7.0	64.6	8.8
0.502	64.6	4.4	54.8	6.7	−0.022	0.053	0.070	0.022	62.5	5.9	64.2	7.6
0.451	62.5	5.3	74.1	7.0	−0.071	0.066	0.054	0.028	53.4	7.9	83.9	7.1
0.401	63.9	5.0	61.8	7.6	−0.040	0.048	0.089	0.018	59.6	7.4	75.3	10.6
0.350	55.4	4.3	78.0	7.5	−0.040	0.049	0.062	0.024	50.0	7.7	89.8	9.2
0.299	60.1	4.5	76.8	7.0	−0.178	0.046	0.053	0.023	36.4	8.9	86.8	6.5
0.249	62.5	3.9	66.5	6.8	−0.021	0.039	0.080	0.029	60.1	5.2	79.6	7.2
0.198	55.2	3.9	82.4	6.6	−0.065	0.042	0.066	0.022	45.9	6.7	95.8	6.2
0.147	43.3	4.7	101.2	6.0	−0.004	0.048	−0.022	0.035	42.5	7.9	95.8	6.4
0.096	38.8	5.1	110.3	6.3	−0.009	0.044	0.032	0.032	37.1	8.3	118.9	7.1
0.046	37.2	5.0	120.6	7.0	−0.028	0.038	0.118	0.034	31.3	9.1	155.6	9.6
−0.005.....	−3.7	4.7	132.0	6.9	−0.051	0.037	0.139	0.034	−15.4	10.7	176.8	11.5
−0.056.....	−24.5	5.4	130.0	7.0	−0.006	0.037	0.010	0.034	−25.9	10.1	133.2	9.7
−0.106.....	−31.6	4.7	103.0	6.0	0.018	0.039	0.028	0.030	−28.4	7.5	110.2	8.4
−0.157.....	−39.2	4.9	92.4	6.8	0.026	0.042	0.076	0.028	−35.0	8.0	109.7	8.5
−0.208.....	−52.1	4.8	87.6	6.5	0.033	0.041	0.033	0.031	−47.1	7.1	94.8	6.4
−0.259.....	−63.7	4.9	79.8	7.0	0.012	0.042	0.062	0.030	−62.1	6.4	91.9	7.9
−0.309.....	−64.2	5.0	67.6	6.5	0.090	0.039	0.068	0.022	−53.7	6.3	78.9	9.0
−0.360.....	−65.6	5.8	68.0	10.4	0.089	0.049	0.122	0.030	−55.1	11.5	88.3	12.4
−0.411.....	−55.7	5.5	65.1	7.8	0.017	0.043	0.102	0.022	−53.8	7.6	81.5	10.8
−0.461.....	−59.9	4.9	58.8	6.3	0.071	0.055	0.067	0.025	−52.7	6.0	68.4	7.4
−0.512.....	−59.0	5.4	50.7	6.4	0.028	0.046	0.061	0.018	−56.5	5.8	58.3	9.8
−0.563.....	−53.9	6.5	72.4	8.5	0.097	0.061	0.058	0.025	−41.7	9.6	82.7	10.4
−0.614.....	−54.2	7.4	67.2	12.0	0.036	0.064	0.127	0.040	−50.0	11.2	88.0	14.8
−0.664.....	−49.5	6.0	49.3	7.6	0.028	0.057	0.077	0.030	−47.1	9.3	58.5	12.2
−0.715.....	−59.2	7.1	61.0	9.4	0.175	0.061	0.069	0.028	−40.7	14.3	71.3	14.1
−0.816.....	−50.8	6.8	55.6	9.5	0.042	0.055	0.113	0.029	−46.8	10.5	71.0	13.8
−0.918.....	−43.3	6.9	58.9	10.1	0.050	0.080	0.101	0.031	−38.2	10.3	73.5	15.2
−1.019.....	−50.7	5.6	60.6	6.8	−0.004	0.065	0.076	0.041	−51.1	8.2	72.0	9.1
−1.121.....	−56.2	6.7	53.3	8.1	0.080	0.073	0.066	0.027	−48.8	14.2	61.9	12.6
−1.252.....	−58.6	7.3	60.2	8.5	0.092	0.072	0.066	0.022	−49.0	10.8	69.9	12.4
−1.425.....	−55.7	9.5	88.1	18.1	0.035	0.077	0.182	0.061	−50.4	17.0	127.4	21.6
−1.658.....	−64.8	6.4	51.2	7.4	0.037	0.058	0.056	0.019	−61.5	9.0	58.2	9.4
−1.932.....	−56.9	8.1	58.0	8.1	0.009	0.094	0.076	0.041	−56.0	9.8	68.8	9.9
−2.257.....	−75.5	9.5	67.2	13.5	0.164	0.096	0.084	0.041	−56.4	17.1	81.1	20.4
−2.642.....	−57.6	10.3	62.1	11.9	0.037	0.105	0.068	0.036	−53.6	15.9	72.5	16.9
−3.078.....	−56.0	9.9	53.8	11.1	0.268	0.106	0.088	0.043	−31.0	17.7	65.4	15.9
−3.555.....	−41.6	27.4	75.6	50.9	0.070	0.283	0.404	0.302	−32.4	34.7	150.3	30.9
−4.194.....	−9.2	15.6	56.4	14.9	−0.144	0.105	0.021	0.037	−22.3	34.1	59.3	20.1
−4.569.....	−39.7	10.8	45.3	9.2	0.240	0.136	0.042	0.036	−20.9	17.4	49.9	13.2

[a] Distance from center of M32 in arcseconds.
[b] Rotation parameter V_0 in km s^{-1}.
[c] Dispersion parameter σ_0 in km s^{-1}.
[d] LOSVD skewness parameter h_3.
[e] LOSVD kurtosis parameter h_4.
[f] $V_{0,c} = V_0 + \sqrt{3}\sigma_0 h_3$, an estimate of the true mean line-of-sight velocity.
[g] $\sigma_{0,c} = \sigma_0(1+\sqrt{6}h_4)$, an estimate of the true line-of-sight velocity dispersion.

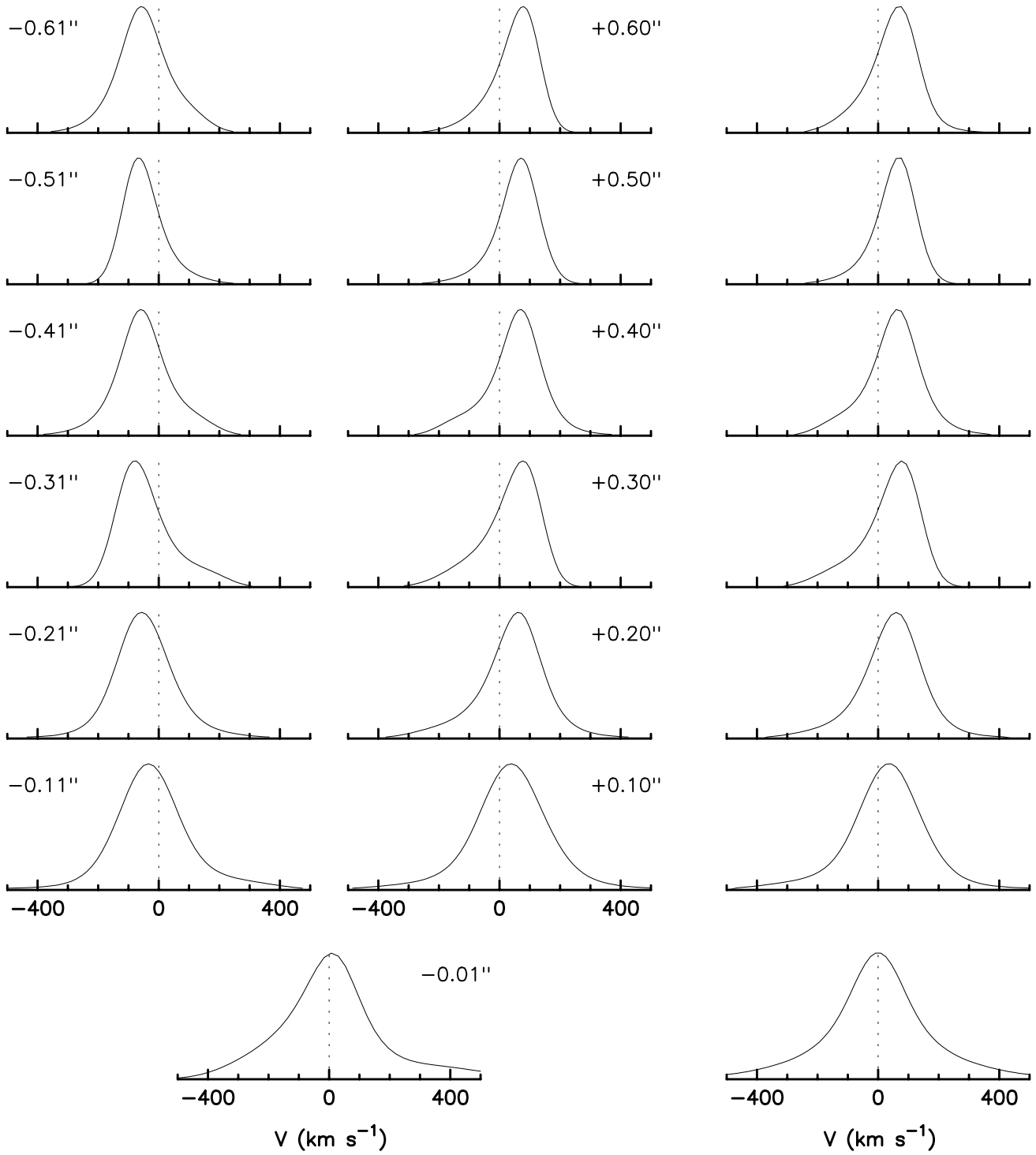

FIG. 4.—Line-of-sight velocity distributions derived from the STIS M32 spectra using the MPL deconvolution algorithm. Note the sudden increase in the width of the broadening functions inside of $\sim 0\farcs2$. The LOSVDs are roughly antisymmetric about the center of M32, as expected for a relaxed system; the right column shows $\hat{N}(V)$ averaged over the left and right sides, $\frac{1}{2}[\hat{N}(V, R) + \hat{N}(-V, -R)]$. The central LOSVD exhibits strong non-Gaussian wings, a likely consequence of high-velocity stars near the central black hole. The broadening functions at larger radii exhibit asymmetries suggestive of a second kinematic subcomponent which rotates with a velocity closer to the systemic velocity of M32.

appears to gradually decline at larger radii. This behavior is similar to that predicted in axisymmetric models (e.g., Fig. 8 of Dehnen 1995), where h_3 remains essentially constant at radii greater than the effective resolution. It is also in good agreement with the h_3 profiles derived from earlier, ground-based studies (van der Marel et al. 1994a; Bender, Kormendy, & Dehnen 1996).

The Gauss-Hermite parameter σ_0 is shown in Figure 6. Also plotted there is h_4, and the "corrected" velocity dispersion, $\sigma_{0,c} = \sigma_0(1 + \sqrt{6}h_4)$; $\sigma_{0,c}$ is a closer approximation than σ_0 to the true rms velocity σ. The velocity dispersion rises suddenly inside of $\sim 0\farcs3$, approximately the same radius at which the rotation curve begins to fall. This coincidence suggests that at least part of the rise in σ_0 is

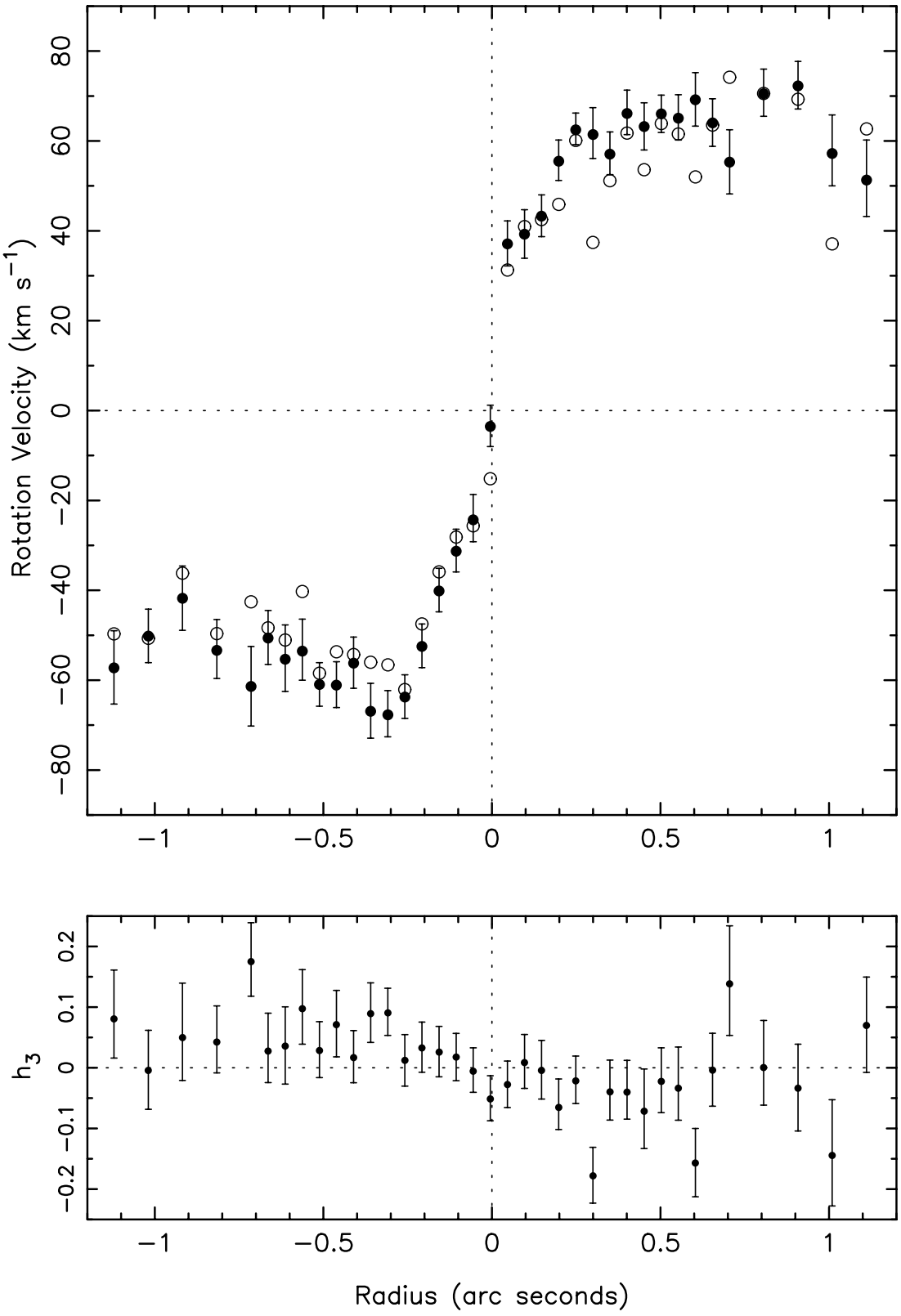

FIG. 5.—STIS rotation curve for M32, derived from LOSVDs obtained using the MPL spectral deconvolution algorithm. *Upper panel*: *filled circles*: V_0, the parameter that measures the velocity shift of the Gaussian function that multiplies the Gauss-Hermite series. *Open circles*: $V_0 + \sqrt{3}\sigma_0 h_3$, an estimate of the true mean line-of-sight velocity. *Lower panel*: the Gauss-Hermite parameter h_3 that measures asymmetries in the LOSVDs. The mean velocity is smaller than $|V_0|$ because of the nonzero value of h_3, which in turn reflects asymmetries in the LOSVDs (Fig. 4).

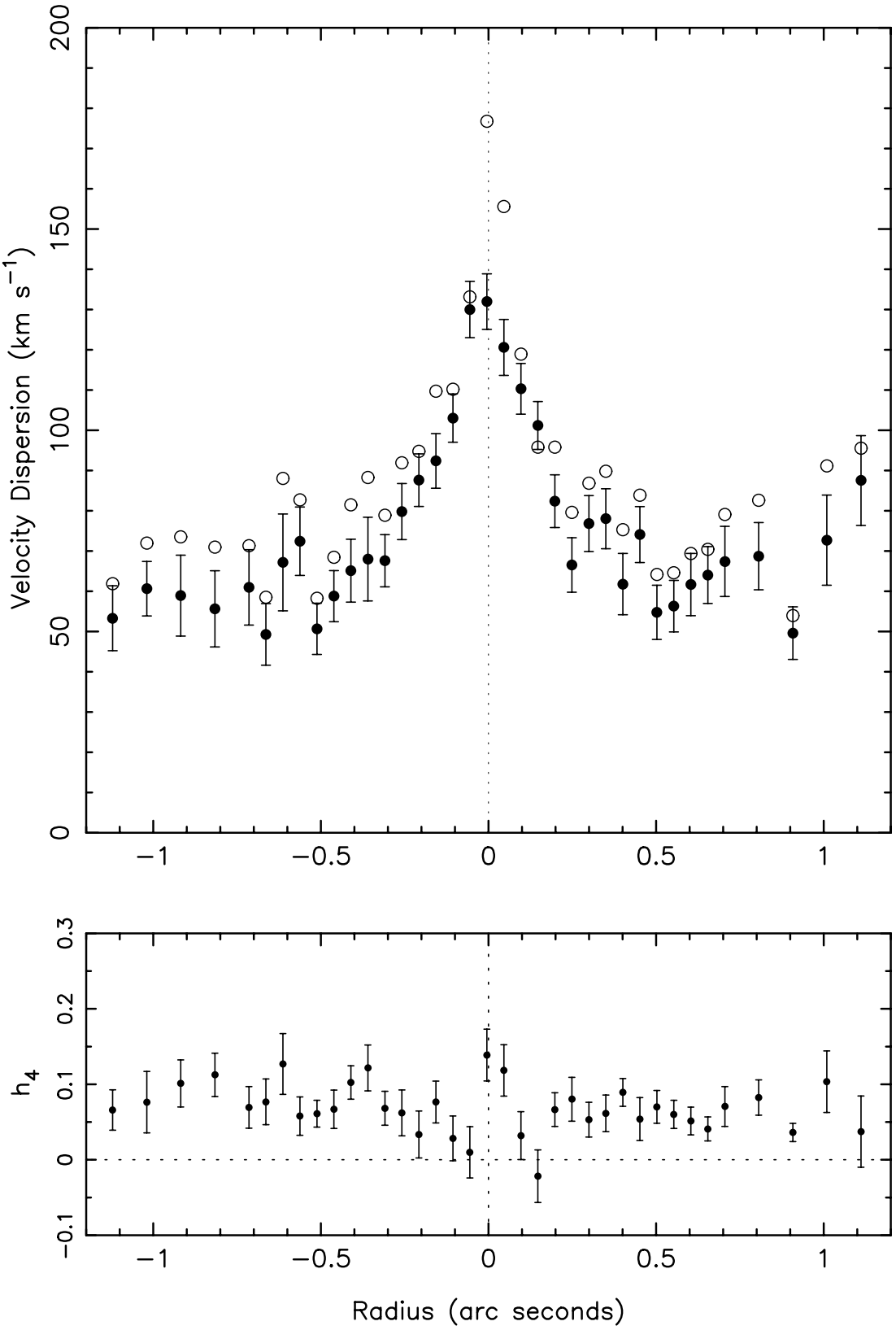

FIG. 6.—STIS velocity dispersion profile for M32, derived from LOSVDs obtained using the MPL spectral deconvolution algorithm. *Upper panel*: *filled circles*: σ_0, the parameter that measures the dispersion of the Gaussian function that multiplies the Gauss-Hermite series. *Open circles*: $\sigma_0(1+\sqrt{h_4})$, an estimate of the true rms line-of-sight velocity. *Lower panel*: the Gauss-Hermite parameter h_4 that measures the amplitude of symmetric non-Gaussian distortions in the LOSVD. The velocity dispersion is generally greater than σ_0 because of to the nonzero values of h_4. This difference is substantial in the inner $\sim 0\farcs2$ because of the strongly non-Gaussian wings of the central LOSVDs (Fig. 4).

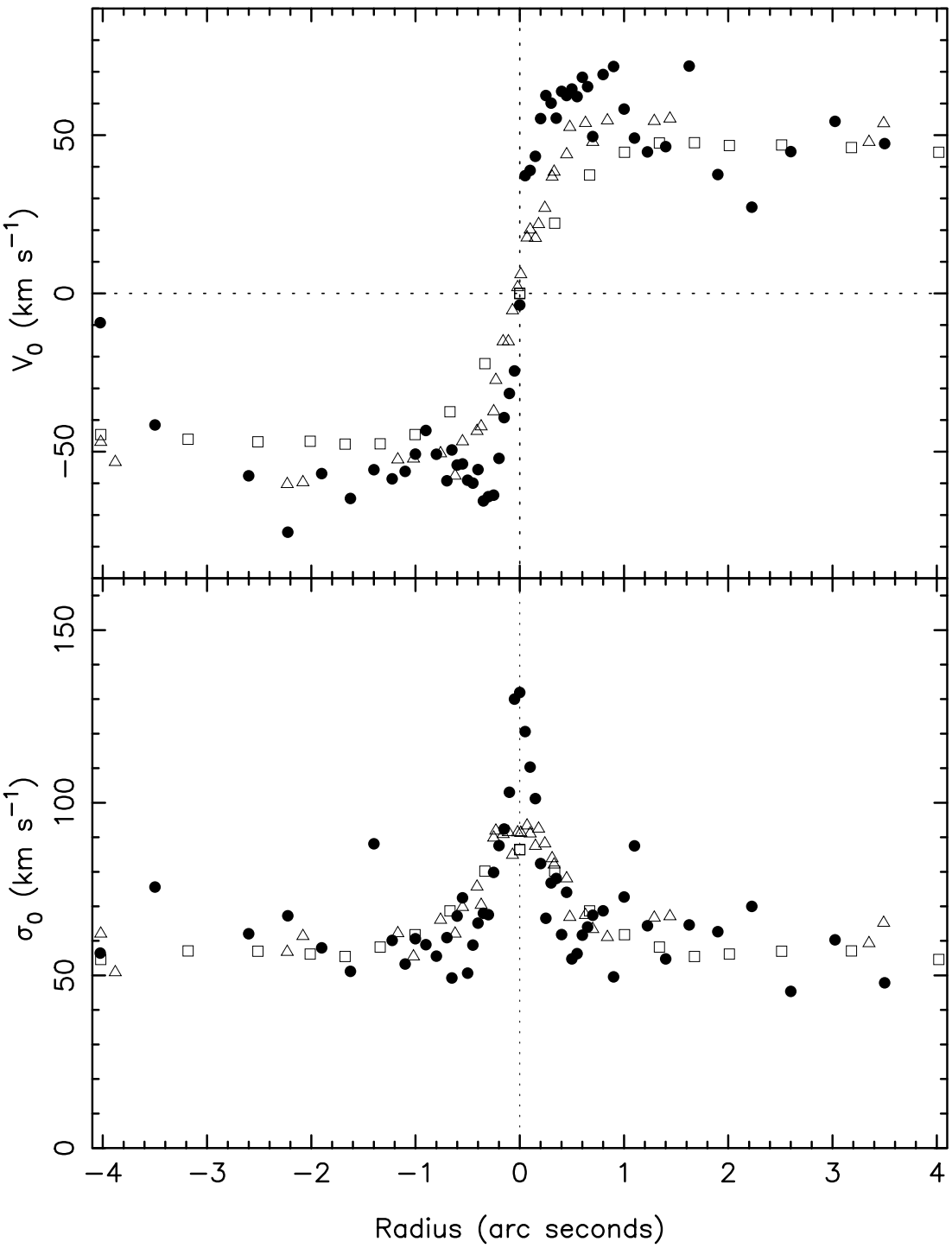

FIG. 7.—Comparison of V_0 and σ_0 derived from the M32 STIS data (*filled circles*) with earlier ground-based determinations. *Squares*: WHT measurements from van der Marel et al. (1994a). *Triangles*: CFHT measurements from Bender et al. (1996).

because of averaging of the rotation velocity over the two sides of the galaxy near the center, which has the effect of converting a rotation into an apparent dispersion (Tonry 1987). We investigate this hypothesis in more detail in the § 3.4.

The corrected velocity dispersion $\sigma_{0,c}$ rises well above σ_0 near the center as a result of the strong non-Gaussian wings of the LOSVD. The central value of $\sigma_{0,c}$ is ~ 175 km s^{-1}; this should probably be interpreted as a lower limit since h_4 is only sensitive to the inner parts of the wings. The ground-based data (Fig. 7) are consistent with the STIS dispersions at radii $\gtrsim 1''$ but fail to resolve the continued rise in σ_0 inside of $\sim 0''.5$.

Dynamical models (e.g., Dehnen 1995; Qian et al. 1995) predict $h_4(R)$ profiles similar to that in Figure 6 when observed with *HST* resolution: a central maximum; a rapid drop, to small or negative values, at $R \approx 0''.1$; and a nearly constant value at larger radii. The predicted drop at $\sim 0''.1$ is

a result of blending of the light from the two sides of the galaxy, which broadens the low-velocity part of the LOSVD and lowers the observed h_4. The predicted central value of h_4 depends strongly on the black hole mass and on the PSF; our value, $\hat{h}_4 \approx 0.14$, is larger than in the two studies just cited, but these studies were based on rather low assumed black hole masses, $M_h = (1\text{–}2) \times 10^6\ M_\odot$. The true black hole mass is probably greater (van der Marel et al. 1998).

The behavior of $\hat{h}_4$ at larger radii is slightly surprising. Previous observational studies (e.g., van der Marel et al. 1994a; Bender, Kormendy, & Dehnen 1996) have returned generally smaller estimates for h_4 in M32. However, we believe that these earlier results are not inconsistent with ours, given the difficulties involved in estimating this parameter. The van der Marel (1994a) study was based on William Hershel Telescope (WHT) observations with a much lower spatial resolution than the STIS data. At radii $\lesssim 1''$, the value of $\hat{h}_4$ recovered by those authors was strongly affected by the PSF blending of the rotation curve discussed above, yielding negative values in the central aperture. Outside of $\sim 2''$, van der Marel et al. (1994a) found $\hat{h}_4$ to increase sharply to ~ 0.03 on both sides of the galaxy (their Fig. 12). Van der Marel (2000, private communication) notes that the values of $\hat{h}_4$ derived from the WHT data depended sensitively on the choice of template spectrum and on the algorithm for continuum subtraction. Using a single, best-fit template, $\hat{h}_4$ was found to lie between ~ 0.03 and ~ 0.05 throughout the inner $\sim 2''$; the lower values of $\hat{h}_4$ in the published paper were derived using an "optimal" template constructed by linear superposition of a set of stellar spectra. We discuss the sensitivity of our results to template mismatch below. In another ground-based study, Bender, Kormendy, & Dehnen (1996) applied the FCQ algorithm to CFHT data of higher spatial resolution and found $\hat{h}_4 \approx 0.05$ inside of $0''.2$, gradually falling to ~ 0 at $\sim 1''.0$. However, the spectral resolution in this study was only 80 km s^{-1} and the derivation of h_3 and h_4 correspondingly difficult; as noted above, we also found $\hat{h}_4 \approx 0$ from the STIS data using the FCQ algorithm and argued that these values were significantly biased.

We may also compare our results to the van der Marel et al. (1997, 1998) *HST*/FOS measurements of V_0 and σ_0 (Fig. 8). The FOS measurements were taken through square apertures as small as $\sim 0''.1$ on a side, hence their spatial resolution is comparable to that of the STIS data. However the FOS is a low-spectral resolution instrument and not well suited to objects like M32 with a relatively low velocity dispersion; furthermore there are difficulties in positioning the FOS and these were probably the cause of the discrepant velocity dispersion measurement of van der Marel et al. One advantage of STIS over FOS is the continuous spatial sampling which avoids potential errors in aperture placement. We find a hint in the STIS data of the asymmetry seen in the FOS $\sigma_0(R)$ profile (a more rapid falloff on the west side). The central FOS value of σ_0 seems significantly bigger than found here, and the FOS rotation velocities are systematically lower.

3.3. *Systematic Errors*

Systematic problems in the spectral deconvolution, template mismatch or incorrect continuum subtraction, can affect the strength of features like the wings and tails seen in the broadening functions of Figure 4 (e.g., van der Marel et al. 1994a). Such errors in most cases would be expected to produce features located at the same velocity on both sides of the galaxy (e.g., Bender, Saglia, & Gerhard 1994) and are therefore an unlikely explanation for the asymmetric tails seen in the off-center LOSVDs. The strong wings and positive $\hat{h}_4$ values might more plausibly be attributed to systematic errors.

We investigated the influence of two possible sources of systematic error on the recovered LOSVDs. The order of the polynomial subtracted from the galaxy and template spectra was varied, from 1 to 5, in order to test the sensitivity of the results to continuum subtraction. The depenence on polynomial order was found to be very slight; the greatest changes occurred in $\hat{h}_4$, but only at a level of a few percent.

Another possible source of systematic error is mismatch between the template spectrum and the unbroadened galaxy spectrum. As discussed above, two additional stellar spectra were available to us, from stars of spectral types G8 and K3; our primary template was type K0. Figure 9 illustrates the effect of varying the template spectrum on the recovery of $\hat{h}_4$ by MPL in the inner $0''.7$ of M32. There are no systematic differences within $\sim 0''.2$, but at larger radii the G8 template produces lower values of $\hat{h}_4$ on average, and the K3 template produces higher values. The fit to the M32 spectra using the primary template was found to be slightly better on average than the fit using the other two templates; however, we made no attempt to derive an "optimal" template by superposition due to the small number of templates available to us.

We also carried out MPL deconvolutions where the fit to the galaxy spectrum was restricted to the region around only one, or two, of the three calcium-triplet lines. The systematic differences were found to be comparable to those obtained with the different templates.

We draw the following conclusions from these tests. Within the central $\sim 0''.2$, both FCQ and MPL give very consistent results for $\hat{h}_4$, and these results depend only weakly on the degree of smoothing, the form of continuum subtraction and the stellar template used. At larger radii, the values of $\hat{h}_4$ recovered by the two algorithms are consistent if the greater biases of the FCQ algorithm are taken into account. However, $\hat{h}_4$ at these radii is moderately dependent on the stellar template used, and the small number of templates available to us does not allow us to rule out h_4 values that are consistent with zero.

3.4. *Interpretation of the Velocity Dispersion Spike*

The velocity dispersion profile (Figs. 6 and 7) exhibits a sudden upturn at a distance of $\sim 0''.3$ from the center, presumably due in part to the gravitational force from a massive compact object. At roughly the same radius, the rotation curve falls (Figs. 5 and 7), presumably because of blending of light from opposite sides of the galaxy which are rotating in opposite directions (in the absence of this blending, the rotation velocity would be expected to diverge as $R^{-1/2}$). The blending should contribute to the rise in the observed velocity dispersion (Tonry 1987), consistent with the fact that the upturn in σ and the drop in $\overline{V}$ occur at roughly the same radius. Here we estimate the degree to which the velocity dispersion spike is a result of this blending.

A number of studies (e.g., Dehnen 1995; van der Marel et al. 1994b) have modeled kinematical data for M32 under

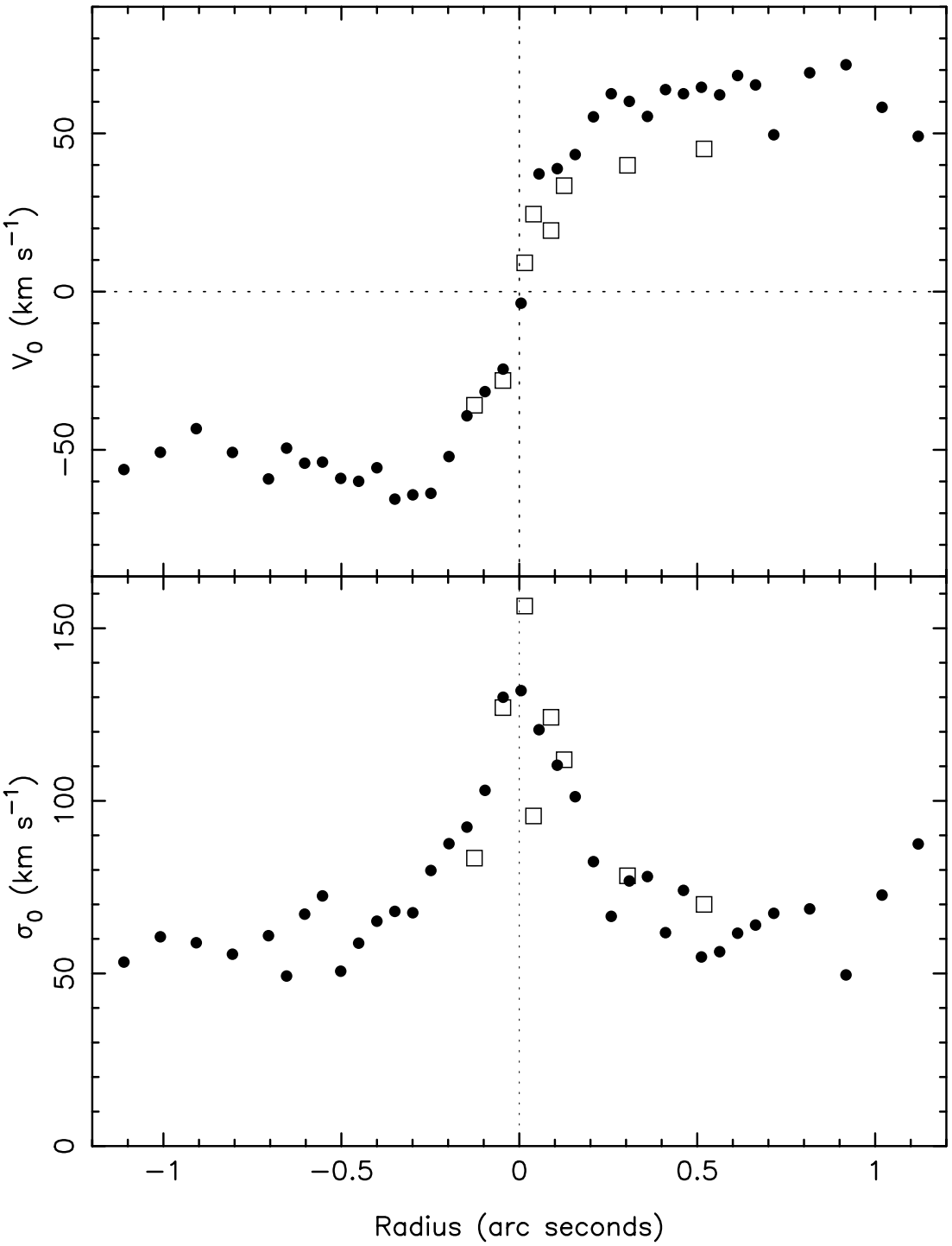

FIG. 8.—Comparison of V_0 and σ_0 derived from the M32 STIS data (*filled circles*) with FOS data of van der Marel et al. (1997) (*open squares*)

the assumption that the stellar distribution function is expressible in terms of the two classical integrals of motion in an axisymmetric potential, $f = f(E, L_z)$. These studies generally conclude that the two-integrable approximation is reasonable for M32. Modeling that relaxes the two-integral assumption (van der Marel et al. 1998) also suggests that the best-fit f is close to the two-integral form $f(E, L_z)$. We therefore make that assumption here. Since our only concern is comparing the predictions of simple models with the kinematics as measured by STIS, there was no need to compute the full phase space density f. Instead we solved the Jeans equations which relate the first and second moments of the velocity distribution to the potential and mass density of the stars, under the assumption of isotropy in the meridional plane (e.g., Fillmore 1986). The stellar luminosity density was assumed to have the form suggested by van der Marel et al. (1998, eq. [1]), a parametrized expression that was fit to photometric data of Lauer et al. (1992) and Kent (1987). The luminosity density was converted into a mass density by the factor $(M/L)(M_\odot/L_\odot)$, with M/L the mass-to-

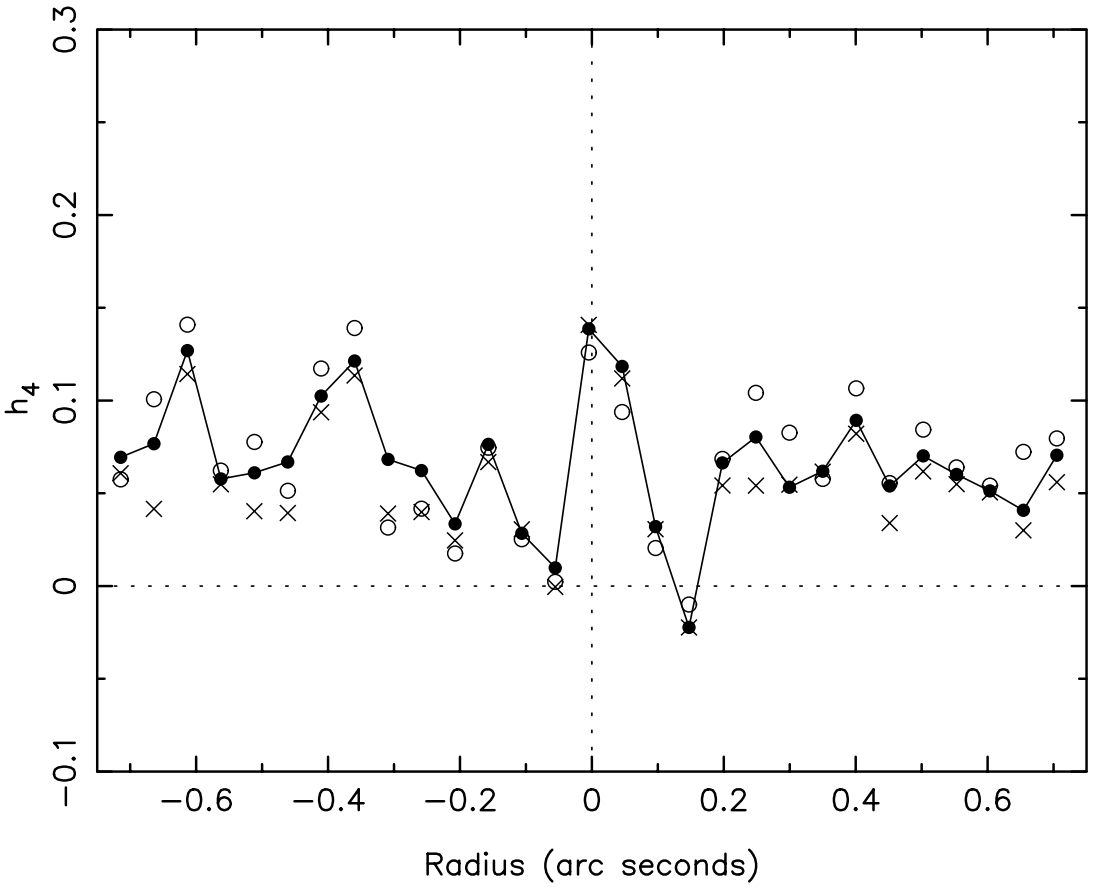

FIG. 9.—Effect of varying the stellar template on the recovery of h_4 using MPL. Filled circles are the same values shown in Fig. 6 (*lower panel*), obtained with the K0 III template star. Open circles correspond to the K3 template and crosses to the G8 template.

light ratio of the stars in solar units. Finally, the gravitational potential was assumed to have the form $\Phi = \Phi_* - GM_h/r$, the combined gravitational potential from the stars and the central black hole. The projected, line-of-sight, mean square velocity $\overline{V^2}$ was then obtained by a density-weighted integration through the galaxy, assumed here to be edge-on (Fillmore 1986). Values of $\overline{V^2}$ were computed on a rectangular grid of 180 × 25 locations with separations of 0.″015 in R and 0.″02 in z. These values were then convolved with the STIS point-spread function (PSF) and averaged over the pixel area and the aperture after weighting by the model surface brightness. The STIS PSF at 8500 Å has an FWHM of ∼0.″115. The PSF is also slightly asymmetric (G. A. Bower et al. 2000, in preparation). We ignored this slight asymmetry.

The second velocity moments of models constructed in this way are uniquely determined by the two parameters (M_h, M/L) that specify the potential. Rather than use the black hole mass estimated by earlier authors, we carried out a χ^2 minimization over the parameters (M_h, M/L), comparing the mean square line-of-sight velocity of the models to that of the data within the inner 1.″0. As estimates of $\overline{V^2}$, we took $V_{0,c}^2 + \sigma_{0,c}^2$, where $V_{0,c}$ and $\sigma_{0,c}$ are the Gauss-Hermite parameters corrected by h_3 and h_4, respectively (Figs. 5 and 6). The best-fit model was found to have $M_h \approx 3.2 \times 10^6\ M_\odot$ and $M/L \approx 3.3$ with $\tilde{\chi}^2 = 0.64$; a $\tilde{\chi}^2$ of unity includes models with M_h as small as $2.2 \times 10^6\ M_\odot$ and as large as $4.3 \times 10^6\ M_\odot$. This range of values is fully consistent with earlier estimates (Dehnen 1995; Bender, Kormendy, & Dehnen 1996; van der Marel et al. 1998).

The rotation of our models may be adjusted by partitioning the azimuthal motions between streaming, $\overline{v_\phi}$, and dispersion, σ_ϕ. We followed the standard practice (Satoh 1980) of making σ_ϕ^2 a weighted average of σ^2 and $\overline{v_\phi^2}$, with the weighting independent of position. When we added this extra freedom to the models and required them to fit the observed rotation and velocity dispersion profiles separately, the best-fit values of (M_h, M/L) were nearly unchanged, but $\tilde{\chi}^2$ increased to 3.7—since the model was now being asked to fit twice as many data points with only one extra parameter. The best-fit models were found to exhibit slightly greater rotation than in an isotropic oblate rotator.

Figure 10 compares the data with the predicted profiles for $M_h = 3.0 \times 10^6\ M_\odot$, close to the best-fit value, and for $M_h = 2.0$ and $4.0 \times 10^6\ M_\odot$. The lowest-order moments of the line-of-sight velocity distribution in M32 are reasonably well fit near the center by our simple axisymmetric model, with a black hole mass $M_h \approx 3 \times 10^6\ M_\odot$. The rotation curve is best fit by a smaller mass [$\sim(1\text{–}2) \times 10^6\ M_\odot$] and the velocity dispersions by a larger mass [$\sim(3\text{–}4) \times 10^6\ M_\odot$]; if we require the models only to fit the mean square velocities, the fit is essentially perfect within the inner arcsecond.

Based on Figure 10, we conclude that the STIS observations probably come close to fully resolving the predicted central rise in the stellar velocity dispersions. This upturn is

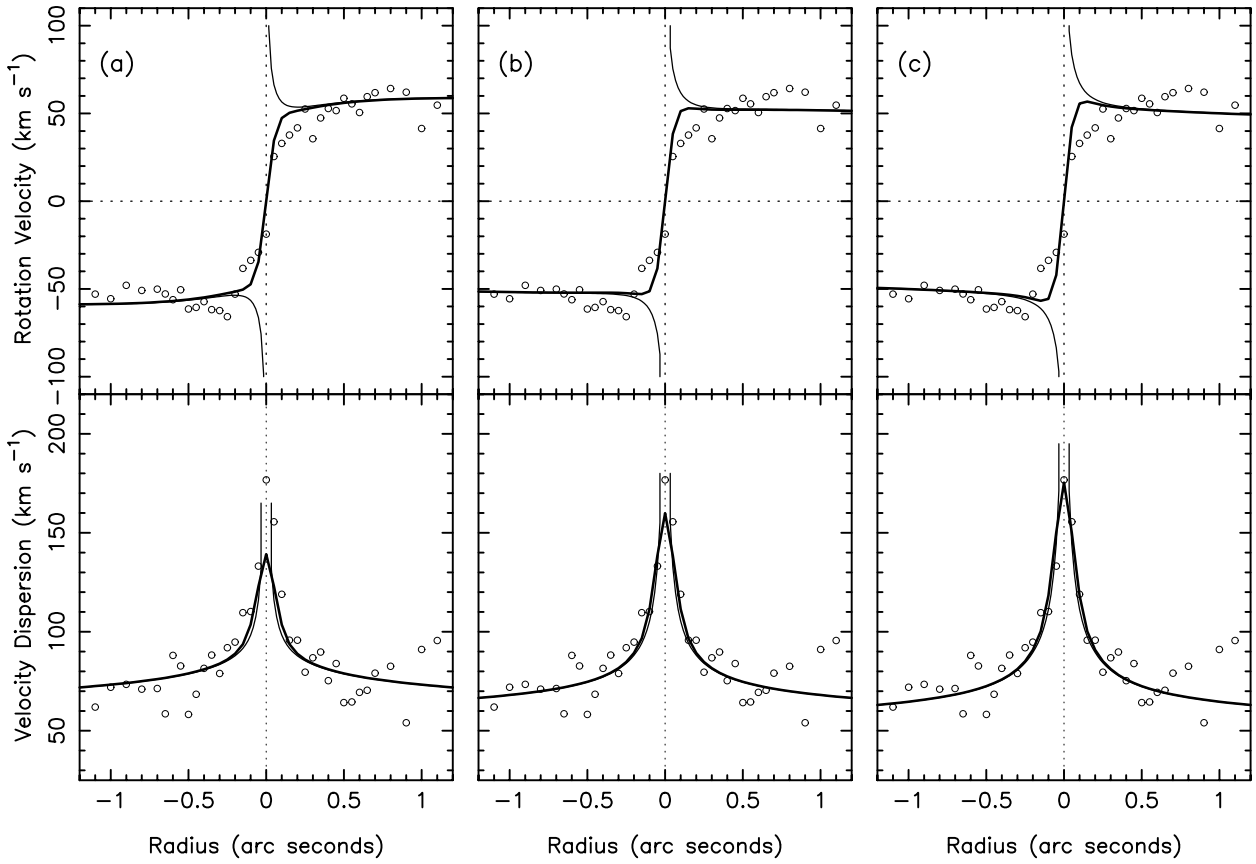

FIG. 10.—Predicted kinematical profiles for three axisymmetric models with different black hole masses. (*a*) $M_h = 2.0 \times 10^6\ M_\odot$; (*b*) $M_h = 3.0 \times 10^6\ M_\odot$; (*c*) $M_h = 4.0 \times 10^6\ M_\odot$. Thin curves show the models as observed with infinite resolution; heavy curves are the models after convolution with the STIS PSF; open circles are the data points. For each M_h, the mass-to-light ratio M/L and rotational parameter k have been adjusted to optimize the fit.

predicted to occur at a projected radius of $\sim 0\farcs1$ for $M_h \sim 2 \times 10^6\ M_\odot$ and $\sim 0\farcs2$ for $M_h \sim 4 \times 10^6\ M_\odot$. Smearing of the stellar rotation field probably accounts for only a small part of the observed velocity dispersion spike.

4. SUMMARY

We used *HST* and STIS to obtain stellar absorption line spectra near the center of M32 in a wavelength region centered on the calcium triplet. The spectra were analyzed using two independent spectral deconvolution routines, FCQ and MPL. The routines gave consistent results for the lowest-order moments of the stellar velocity distribution, but systematically different results for h_4; we argued that the differences could be reconciled after taking into account the different biases of the two algorithms. The stellar rotation velocities in M32 are slightly higher than observed from the ground and remain constant into $\sim 0\farcs25$ from the center. The velocity dispersions exhibit a clear spike beginning at approximately the same radius. While part of the rise in the velocity dispersion is an artifact of blending of the rotation curve from the two sides of the galaxy, we argued based on comparision with models that most of the velocity dispersion spike reflects a true rise in the random stellar velocity, due presumably in part to the presence of a black hole.

Detailed dynamical modeling of M32 based on these data and estimates of the black hole mass will be presented in Paper II.

We thank W. Dehnen and R. van der Marel for helpful discussions. This work was supported by NASA grants NAG 5-3158 and NAG 5-6037, by NSF grant AST 96-17088, and by STIS GTO funding. Data presented here were based on observations with the NASA/ESA *Hubble Space Telescope*, obtained at the Space Telescope Science Institute, which is operated by the Association of Universities for Research in Astronomy, Inc. (AURA), under NASA contract NAS 5-26555.

APPENDIX A

GAUSS-HERMITE MOMENTS

The two spectral deconvolution algorithms described above yield nonparametric estimates $\hat{N}(V)$ of the stellar LOSVD. Here we describe the methods used by the two algorithms to derive the GH moments from $\hat{N}(V)$.

Let $N(X, Y; V)$ be the distribution of line-of-sight stellar velocities in the aperture centered at (X, Y). Define the GH

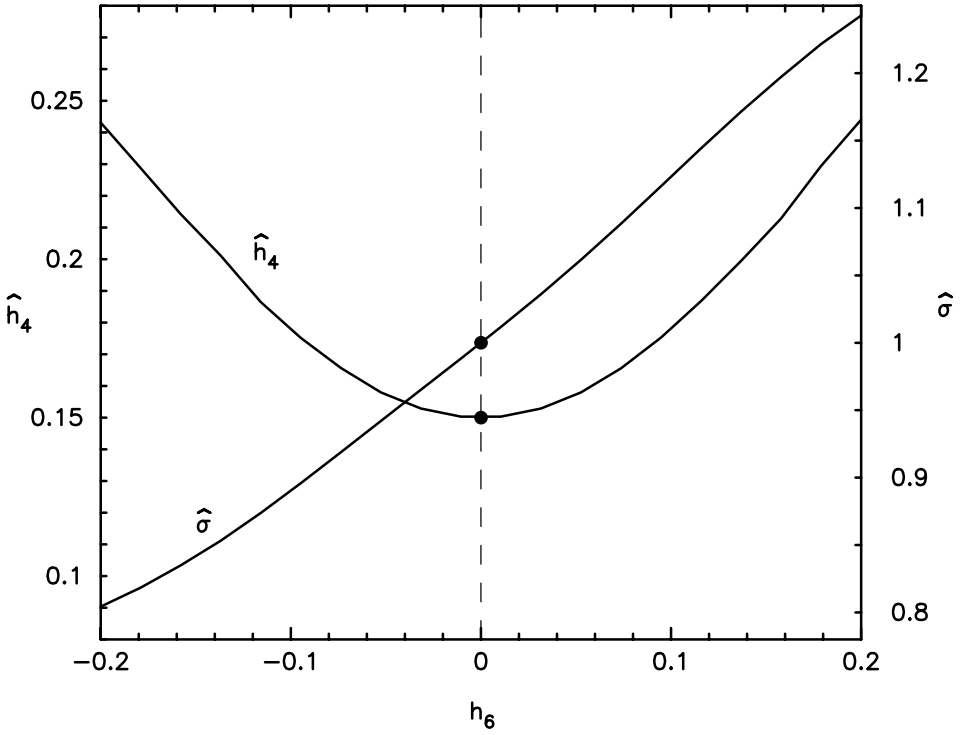

FIG. 11.—Estimated Gauss-Hermite parameters $\hat{\sigma}$ and $\hat{h}_4$, derived by fitting the $N(V)$ of eq. (A6) to the assumed form (A5), with $j_{\max} = 4$. Filled circles indicate the input values of σ_0 and h_4; these values are recovered only when the input $N(V)$ has $h_6 = 0$.

moments of N as

$$h_i(X, Y) = 2\sqrt{\pi} \int_{-\infty}^{\infty} N(X, Y; V) g(w) H_i(w) dV , \tag{A1}$$

where H_i are the Hermite polynomials (as defined by Gerhard 1993) and the weight function

$$g(w) = \frac{1}{\sqrt{2\pi}\gamma_0} e^{-w^2/2} , \qquad w = (V - V_0)/\sigma_0 , \tag{A2}$$

has three free parameters (γ_0, V_0, σ_0). Following van der Marel & Franx (1993), we choose these parameters at every point (X, Y) such that

$$h_0(X, Y) = 1 , \qquad h_1(X, Y) = h_2(X, Y) = 0 . \tag{A3}$$

These definitions impose the following implicit conditions on (γ_0, V_0, σ_0)

$$\gamma_0 = \sqrt{2}\sigma_0 \int_{-\infty}^{\infty} N(V) e^{-w^2/2} dw , \tag{A4a}$$

$$0 = \int_{-\infty}^{\infty} N(V) e^{-w^2/2} w \, dw , \tag{A4b}$$

$$0 = \int_{-\infty}^{\infty} N(V) e^{-w^2/2} (2w^2 - 1) dw . \tag{A4c}$$

The relations (A4a)–(A4c) define a nonlinear minimization problem with solutions (γ_0, V_0, σ_0) given $N(V)$.

The MPL algorithm (Merritt 1997) derives the three parameters in just this way, using the NAG routine E04FDF to minimize the sum $(h_0 - 1)^2 + h_1^2 + h_2^2$ as a function of (γ_0, V_0, σ_0). The higher order GH moments are then derived using equation (A1), by numerical integration over $\hat{N}(V)$.

Most spectral deconvolution algorithms of which we are aware derive the parameters (γ_0, V_0, σ_0) in a different way. The LOSVD is compared to the trial function

$$\mathcal{N}(V) = \frac{\gamma_0}{\sqrt{2\pi}\sigma_0} e^{-w^2/2} \left[1 + \sum_{j=3}^{j_{\max}} h_j H_j(w) \right] , \tag{A5}$$

where $j_{\max}$ is the index of the highest GH moment fitted to $\hat{N}(V)$; typically $j_{\max} = 4$. The integrated square deviation between $\hat{N}(V)$ and $\mathcal{N}(\mathcal{V})$ is then minimized by varying the $(j_{\max} + 1)$ free parameters $(\gamma_0, V_0, \sigma_0, h_3, h_4, \ldots, h_{j_{\max}})$. This is the technique used by the FCQ algorithm.

A theorem (Myller-Lebedeff 1908) guarantees the equivalence of the two approaches if $j_{\max} = \infty$ in equation (A5) (van der Marel & Franx 1993). However, if $j_{\max} \neq \infty$, and if the input $N(V)$ can not be precisely represented by a finite GH series with $j \leq j_{\max}$, the results given by the two algorithms will differ. For instance, in attempting to represent an $N(V)$ having $h_6 \neq 0$ using $j_{\max} = 4$, the FCQ algorithm will adjust σ_0 and h_4 to incorrect values in order to better fit the high-velocity wings of the profile with the limited number of terms allowed to it. This is illustrated in Figure 11, which shows the values of σ_0 and h_4 generated by the second algorithm, $\hat{\sigma}_0$ and $\hat{h}_4$, compared to the true values for an input $N(V)$ with $h_4 = 0.15$ and nonzero h_6:

$$N(V) = \frac{1}{\sqrt{2\pi}} e^{-V^2/2}[1 + 0.15H_4(V) + h_6 H_6(V)] . \tag{A6}$$

For $|h_6| \gtrsim 0.1$, the errors in σ_0 and h_4 as derived from the second algorithm are $\gtrsim 15\%$ and $\gtrsim 20\%$, respectively. While the value of h_6 is not easy to determine in real galaxies, most studies (e.g., van der Marel et al. 1994a; Bender, Kormendy, & Dehnen 1996) suggest values much smaller than required to significantly influence the determination of h_4.

APPENDIX B

PERFORMANCE EVALUATION OF THE FCQ AND MPL ALGORITHMS

Here we compare the performance of the FCQ and MPL algorithms given simulated data. Our primary goal is to understand the source of the systematic offset of h_4 values as derived from the M32 spectra by the two algorithms (§ 3.1). Two independent sets of tests were carried out, the first by R. Bender and the second by D. Merritt. All tests were based on synthesized galaxy spectra generated from the STIS template spectrum (Fig. 1) by convolving it with an assumed $N(V)$ and adding noise.

The first set of tests addressed the accuracy of FCQ estimates when the galaxy velocity dispersion is low. It is well known that the accuracy of FCQ begins to fall off when the galaxy velocity dispersion becomes comparable to the dispersion of the template spectrum (e.g., Bender, Paquet, & Nieto 1991). Figure 12 shows values of $\hat{\sigma}_0$ recovered by FCQ given a Gaussian-broadened template spectrum and thirty random noise realizations. The default value ($W \approx 1$) of the smoothing parameter was used. There is a positive bias in the estimated values beginning at $\sigma_0 \approx 100$ km s^{-1}; the bias increases with decreasing σ_0 becoming significant for $\sigma_0 \approx 50$ km s^{-1}. The bias is only weakly dependent on S/N. This bias in the estimation of σ_0 is unlikely to be important for the nucleus of M32 where $\sigma_0 \gtrsim 100$ km s^{-1}.

Figure 13 shows the performance of FCQ at recovering h_4. The template spectrum was broadened using an $N(V)$ of the form

$$N_1(V) = \frac{1}{\sqrt{2\pi}} e^{-V^2/2\sigma_0^2}[1 + h_4 H_4(V/\sigma_0)] , \tag{B1}$$

with various values of σ_0 and h_4. Figure 13 reveals significant biases in $\hat{h}_4$ for $\sigma_0 \lesssim 100$ km s^{-1}, even when the S/N is as great as 100. When $\sigma_0 \approx 50$ km s^{-1} and S/N ≈ 30, characteristic of M32 at $\sim 1''$, the bias in h_4 is ~ -0.1 for an input h_4 of ~ 0.1.

The second set of tests compared the performance of the FCQ and MPL algorithms on galaxy spectra generated from the broadening function

$$N_2(V) = \frac{1}{\pi\sigma} \frac{1}{1 + (V/\sigma)^2} , \tag{B2}$$

a Lorentzian function, with $\sigma = 100$ km s^{-1}. This LOSVD is qualitatively similar to what is expected in a black hole cusp, with $N \sim V^{-2}$ high-velocity wings. The nontrivial GH parameters are

$$\gamma_0 = 0.76986 , \qquad \sigma_0 = 108.07 \text{ km s}^{-1} , \qquad h_4 = 0.14546 , \qquad h_6 = 0.01850 . \tag{B3}$$

Figure 14 shows mean estimates of $N(V)$ obtained using the two algorithms for 100 random realizations of the noise. The smoothing parameter in both algorithms was adjusted to minimize the mean square error of $\hat{N}(V)$ (as defined below) for each value of S/N. There is a greater bias in the FCQ estimates, as well as a persistent "ringing" at high velocities.

Figure 15 plots the mean integrated square error (MISE) and integrated square bias (ISB) of the recovered broadening functions as functions of S/N; in the case of the FCQ algorithm, the integrated errors are shown both for the optimal choice of smoothing parameter W_{opt} that minimizes the MISE, as well as for the value chosen by the algorithm (~ 1.3). The MISE of an estimate $\hat{f}(x)$ is defined as

$$\text{MISE}[\hat{f}(x)] = E \int \{\hat{f}(x) - f(x)\}^2 dx \tag{B4a}$$

$$= \int \{E\hat{f}(x) - f(x)\}^2 dx + \int \{E[\hat{f}^2(x)] - E[\hat{f}(x)^2]\} dx \tag{B4b}$$

$$= \text{ISB}[\widehat{f(x)}] + \text{IV}[\widehat{f(x)}] , \tag{B4c}$$

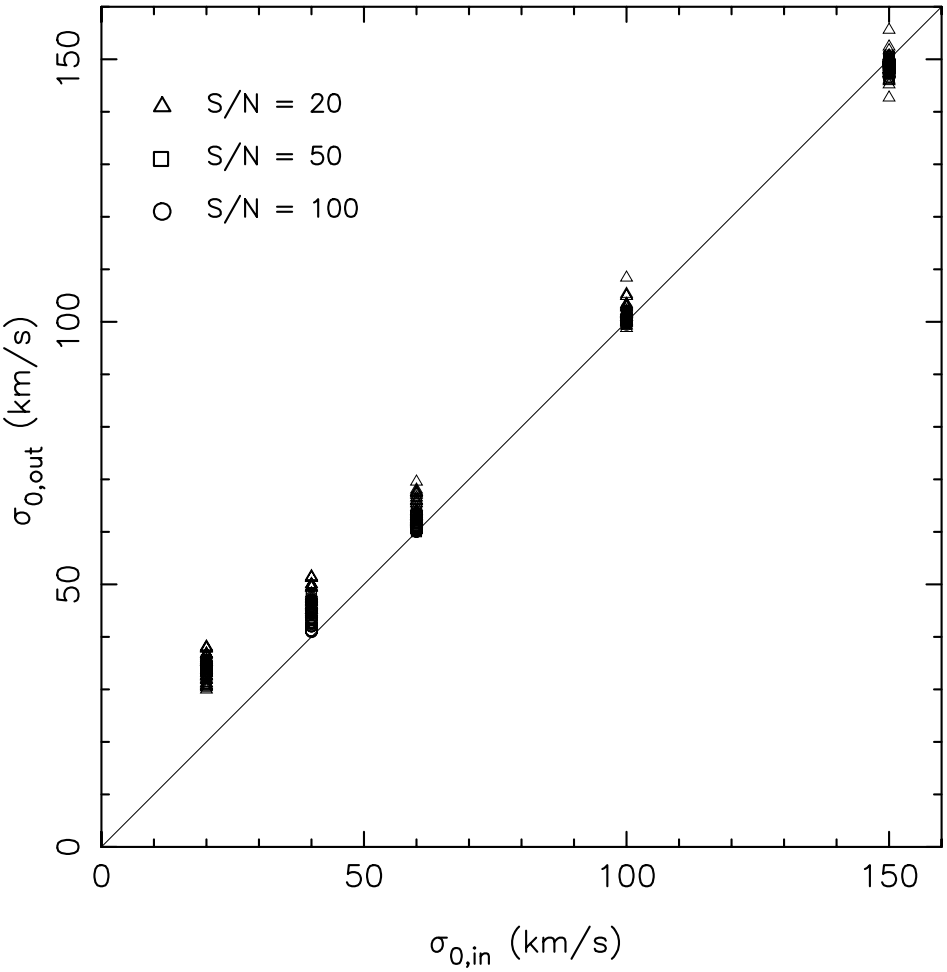

FIG. 12.—Recovery of σ_0 via FCQ

the sum of the integrated square bias ISB and the integrated variance IV (Silverman 1986); here E denotes the expectation value, i.e., the average over many random realizations of the noise. The MISE and ISB displayed in Figure 15 were divided by the normalizing factor $\int [N_2(V)]^2\, dV$.

The MISE of the MPL estimates falls roughly as a power law, $\mathrm{MISE}[\hat{N}(V)] \sim (\mathrm{S/N})^{-1.3}$, close to the asymptotic $(\mathrm{S/N})^{-1}$ of parametric estimators. Approximately $\frac{1}{2}$ of the total square error comes from the bias and $\frac{1}{2}$ from the variance. In the case of

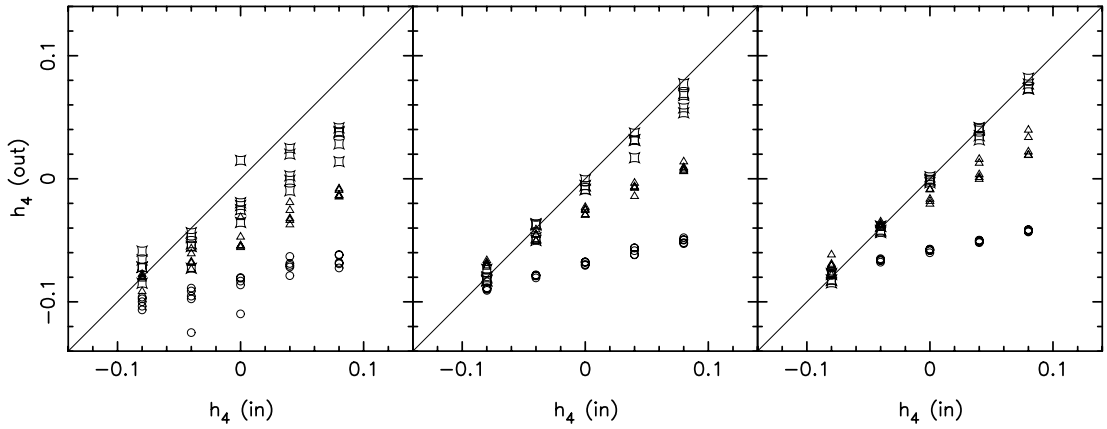

FIG. 13.—Recovery of h_4 via FCQ. *Circles*: $\sigma_0 = 40$ km s^{-1}. *Triangles*: $\sigma_0 = 60$ km s^{-1}. *Squares*: $\sigma_0 = 100$ km s^{-1}. There is a significant negative bias in the recovered values of h_4 when the velocity dispersion is less than about 100 km s^{-1}.

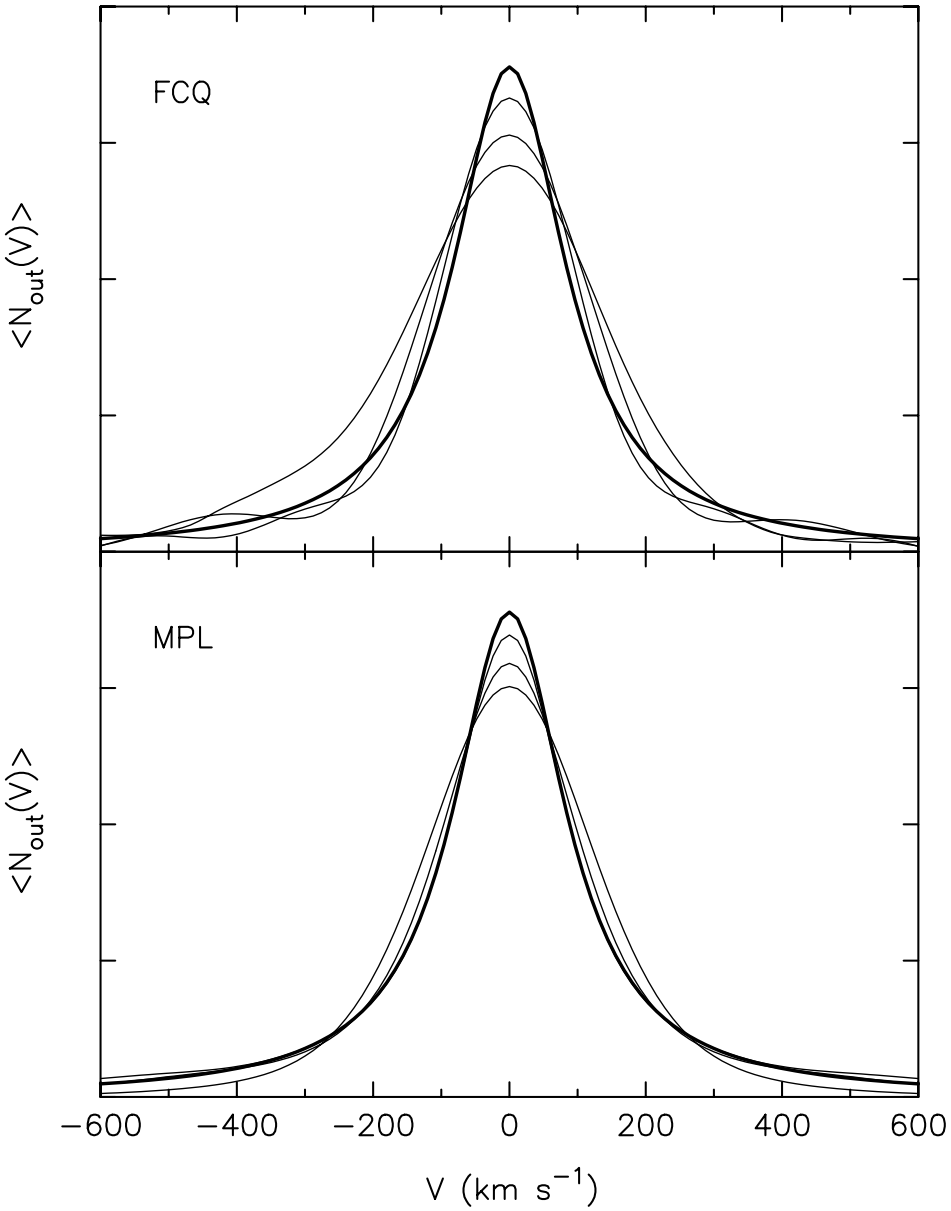

FIG. 14.—Mean estimates of $N(V)$ averaged over 100 random realizations of the observed spectrum, for S/N $= \{5,20,100\}$. The input $N(V)$ (eq. [B2]) is shown by the heavy curves.

the FCQ algorithm, the MISE behaves in a more complicated way with S/N, at first falling with S/N then appearing to level off for S/N $\gtrsim 50$. This levelling off is a consequence of the low-velocity-dispersion bias of FCQ discussed above. For the FCQ estimates, the bulk of the MISE is a result of the variance; adjusting the smoothing parameter primarily affects the bias and has little effect on the MISE. For S/N ≈ 20, the mean square error of the optimal FCQ estimate is a factor ~ 3 greater than that of the MPL estimates.

The bias in $\hat{N}(V)$ is in the direction of wider and more steeply truncated functions, particularly in the case of the FCQ estimates (Fig. 14). This bias in $\hat{N}(V)$ is consistent with the negative bias found above in estimates of h_4. Figure 16 compares the ability of the two algorithms to recover h_4 from the Lorentzian $N_2(V)$. Plotted there are the mean square error (MSE) and bias in estimates of h_4 from 100 random noise realizations; the MSE is defined, for any estimated parameter $\hat{P}$, as

$$\mathrm{MSE}(\hat{P}) = E\{\hat{P} - P\}^2 , \tag{B5}$$

which can also be decomposed into contributions from the squared bias SB and the variance V:

$$\mathrm{MSE}(\hat{P}) = (E\hat{P} - P)^2 + (E\{\hat{P}^2\} - E\{\hat{P}\}^2) \tag{B6a}$$

$$= \mathrm{SB}(\hat{P}) + V(\hat{P}) . \tag{B6b}$$

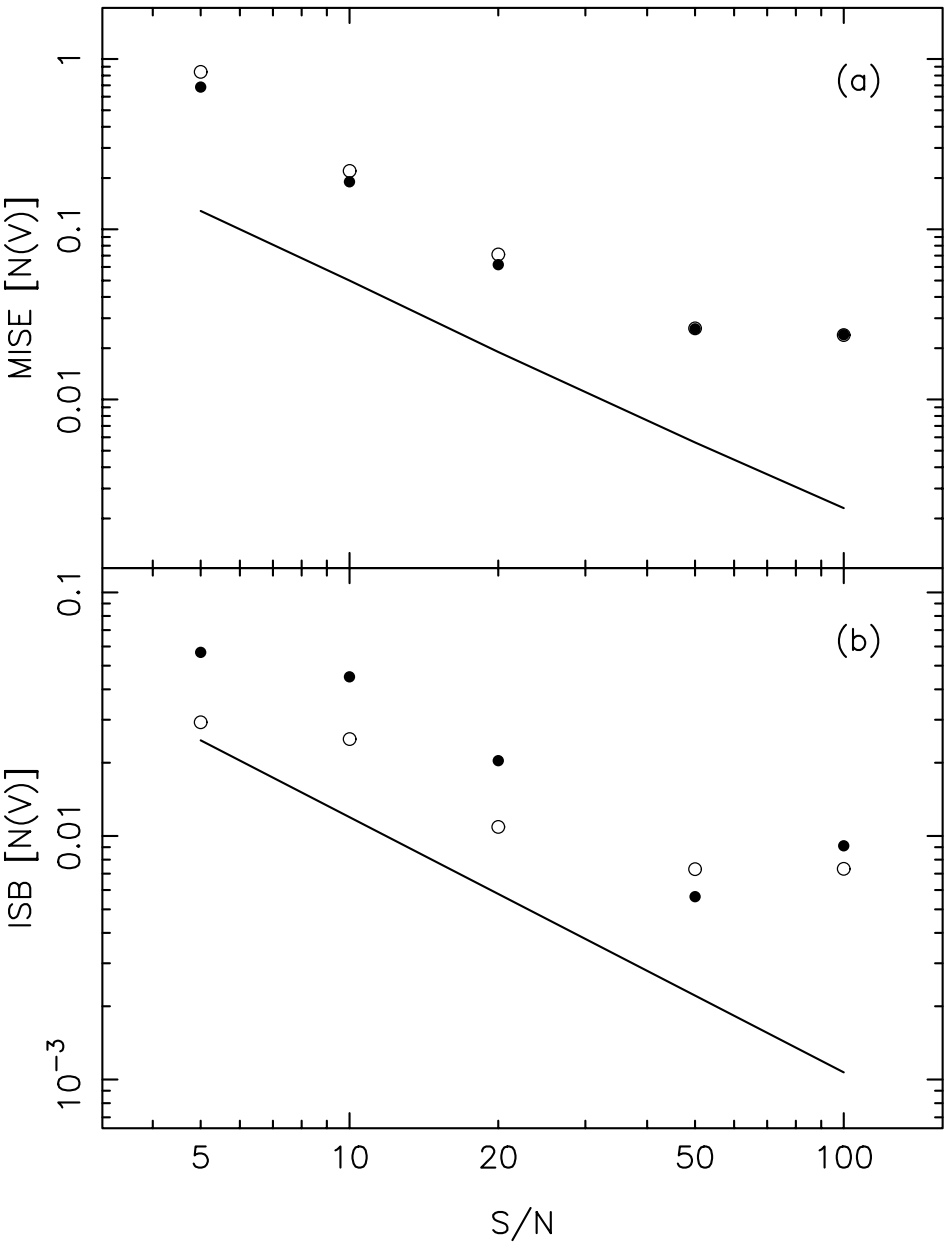

FIG. 15.—MISE and ISB of estimates of $N(V)$ obtained from the two deconvolution algorithms. The input LOSVD was a Lorentzian (eq. [B2]) with $\sigma_0 = 108$ km s^{-1} and $h_4 = 0.15$. Both MISE and ISB have been normalized as described in the text. *Solid lines*: MPL algorithm. *Open circles*: FCQ algorithm, using a fixed smoothing parameter $W = 1.3$. *Filled circles*: FCQ algorithm, using the value $W_{\rm opt}$ that minimizes the MISE of the estimated $N(V)$.

The MSE of estimates obtained with the MPL algorithm again varies roughly as a power law, $\mathrm{MSE}(\hat{h}_4) \sim (S/N)^{-1.5}$. The bias in the MPL estimates is always negative, i.e. in the direction of more Gaussian $N(V)$'s; for $S/N \sim 20$, this bias is a modest ~ -0.03, dropping to $\lesssim -0.01$ for S/N = 100.

The FCQ estimates of h_4 show a considerably greater error, both in the bias and the variance. Two sets of FCQ estimates were made: first using the default value of the smoothing parameter returned by the code, $W \approx 1.3$; and second using the optimum value $W_{\rm opt}$ that minimized the MSE of the h_4 estimates at each S/N. For the default value of W, the algorithm returns mean estimates of h_4 that lie in the range 0.03–0.05 for all values of S/N $\geq$ 10, an average error of $\sim$70%. However the optimum smoothing parameter for the recovery of h_4 was found to vary strongly with S/N, from $W_{\rm opt} \sim 0.5$ for S/N = 5 to $W_{\rm opt} \sim 2$ for S/N = 100 (Fig. 16, panel *c*). Nevertheless a substantial bias remains when $W_{\rm opt}$ is used, of order ~ -0.05 even for S/N = 50–100. These biases are larger than found above using a more Gaussian $N(V)$ with smaller h_4 and suggest that FCQ estimates of h_4 may be substantially biased even for σ_0 as large as $\sim$100 km s^{-1} when the true $N(V)$ is sufficiently non-Gaussian.

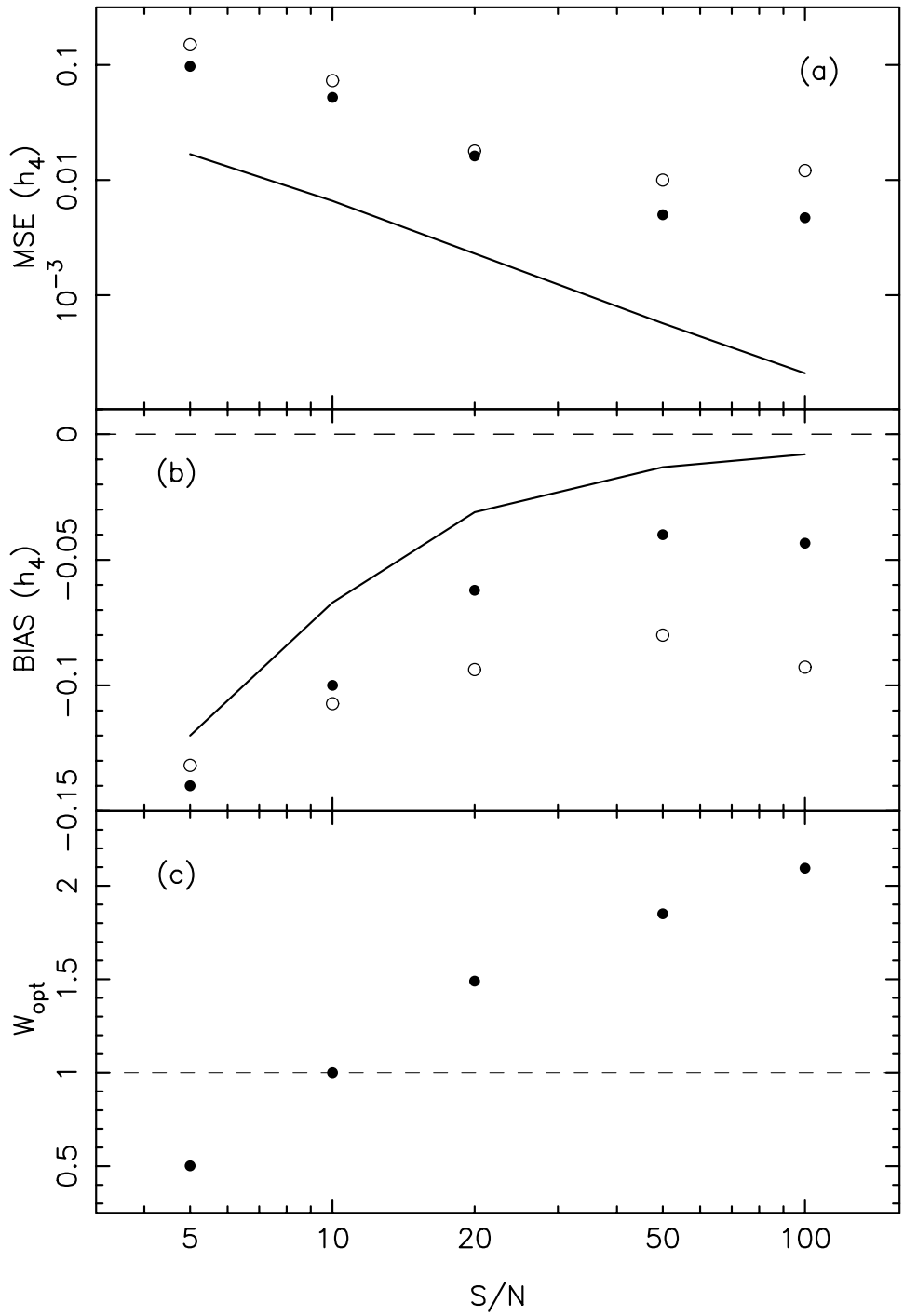

FIG. 16.—MSE and bias in estimates of h_4 obtained from the two deconvolution algorithms. The input $N(V)$ was a Lorentzian (eq. [B2]) with $\sigma_0 = 108$ km s^{-1} and $h_4 = 0.15$. *Solid lines*: MPL algorithm. *Open circles*: FCQ algorithm, with $W = 1.2$. *Filled circles*: FCQ algorithm, using the value W_{opt} that minimizes the MISE of the estimate $\hat{h}_4$. W_{opt} is plotted vs. S/N in the bottom panel.

REFERENCES

Bahcall, J., & Wolf, S. 1976, ApJ, 209, 214
Bender, R. 1990, A&A, 229, 441
Bender, R., Kormendy, J., & Dehnen, W. 1996, ApJ, 464, L123
Bender, R., Paquet, A., & Nieto, J.-L. 1991, A&A, 246, 349
Bender, R., Saglia, R., & Gerhard, O. 1994, MNRAS, 269, 785
Carter, D., & Jenkins, C. R. 1993, MNRAS, 263, 1049
Dehnen, W. 1995, MNRAS, 274, 919
Dressler, A., & Richstone, D. O. 1988, ApJ, 324, 701
Fillmore, J. A. 1986, AJ, 91, 1096
Gebhardt, K., et al. 2000, AJ, 119, 1157
Gerhard, O. E. 1993, MNRAS, 265, 213
Goudfrooij, P., Baum, S. A., & Walsh, J. R. 1997, in The 1997 *HST* Calibration Workshop with a New Generation of Instruments (Baltimore: STScI), 100
Kimble, R. A., et al. 1998, ApJ, 492, L83
Lauer, T. R., et al. 1992, AJ, 104, 552
Merritt, D. 1997, AJ, 114, 228
Myller-Lebedeff, W. 1908, Math. Ann. 64, 388

Peebles, P. J. E. 1972, Gen. Relativ. Gravitation, 3, 63
Qian, E. E., de Zeeuw, P. T., van der Marel, R. P., & Hunter, C. 1995, MNRAS, 274, 602
Sargent, W. L. W., Schechter, P. L., Boksenberg, A., & Shortridge, K. 1977, ApJ, 212, 326
Satoh, C. 1980, PASJ, 32, 41
Silverman, B. W. 1982, Ann. Stat. 10, 795
———. 1986, Density Estimation for Statistics and Data Analysis (Chapman & Hall: London)
Thompson, J. R., & Tapia, R. A. 1990, Nonparametric Function Estimation, Modeling, and Simulation (Philadelphia: SIAM), 37
Tonry, J. L. 1987, ApJ, 322, 632
van der Marel, R. 1994, ApJ, 432, L91
van der Marel, R. P., Cretton, N., de Zeeuw, P. T., & Rix, H. W. 1998, ApJ, 493, 613
van der Marel, R. P., de Zeeuw, P. T., & Rix, H. W. 1997b, ApJ, 488, 119
van der Marel, R. P., de Zeeuw, P. T., & Rix, H. W. & Quinlan, G. D. 1997a, Nature, 385, 610
van der Marel, R. P., & Franx, M. 1993, ApJ, 407, 525
van der Marel, R. P., Rix, H.-W., Carter, D., Franx, M., White, S. D. M., & de Zeeuw, T. 1994a, MNRAS, 268, 521
van der Marel, R. P., Wyn-Evans, N., Rix, H.-W., White, S. D. M., & de Zeeuw, T. 1994b, MNRAS, 271, 99
Woodgate, B. E., et al. 1998, PASP, 110, 1183